Received: 22 November 2023 | Revised: 4 August 2024 | Accepted: 21 August 2024

DOI: 10.1002/cac2.12608

CANCER COMMUNICATIONS Open Access

ORIGINAL ARTICLE

Tryptophan 2,3-dioxygenase-positive matrix fibroblasts fuel breast cancer lung metastasis via kynurenine-mediated ferroptosis resistance of metastatic cells and T cell dysfunction

Yongcan Liu[1] | **Shanchun Chen**[1] | **Xueying Wan**[1] | **Rui Wang**[1] | **Haojun Luo**[2] | **Chao Chang**[1] | **Peijin Dai**[1] | **Yubi Gan**[1] | **Yuetong Guo**[1] | **Yixuan Hou**[3] | **Yan Sun**[4] | **Yong Teng**[5,6] | **Xiaojiang Cui**[7] | **Manran Liu**[1]

[1]Key Laboratory of Laboratory Medical Diagnostics, Chinese Ministry of Education, Chongqing Medical University, Chongqing, P. R. China

[2]Department of Thyroid and Breast Surgery, The Second Affiliated Hospital of Chongqing Medical University, Chongqing, P. R. China

[3]Experimental Teaching Center of Basic Medicine Science, Chongqing Medical University, Chongqing, P. R. China

[4]Department of Cell Biology and Medical Genetics, Basic Medical School, Chongqing Medical University, Chongqing, P. R. China

[5]Department of Hematology and Medical Oncology, Winship Cancer Institute, Emory University School of Medicine, Atlanta, Georgia, USA

[6]Wallace H. Coulter Department of Biomedical Engineering, Georgia Institute of Technology and Emory University, Atlanta, Georgia, USA

[7]Department of Surgery, Department of Obstetrics and Gynecology, Samuel Oschin Comprehensive Cancer Institute, Cedars-Sinai Medical Center, Los Angeles, California, USA

Correspondence
Manran Liu, Key Laboratory of Laboratory Medical Diagnostics, Chinese Ministry of Education, Chongqing Medical University, Chongqing 400016, P. R. China.
Email: manranliu@cqmu.edu.cn

Abstract

Background: Tumor metastasis is a major threat to cancer patient survival. The organ-specific niche plays a pivotal role in tumor organotropic metastasis. Fibroblasts serve as a vital component of the metastatic microenvironment, but how heterogeneous metastasis-associated fibroblasts (MAFs) promote

List of abbreviations: AKR1C1, aldo-keto reductase family 1 member C1; APC, allophycocyanine; CCL8/9/11/19, C-C motif chemokine ligand 8/9/11/19; CD31, cluster of differentiation 31; CM, conditioned medium; CNV, copy number variation; *CTLA4*, cytotoxic T-lymphocyte associated protein 4; DEGs, differentially expressed genes; DTCs, disseminated tumor cells; FACS, fluorescence-activated cell sorting; FBS, fetal bovine serum; *Fth1*, ferritin heavy chain 1; GFP, green fluorescent protein; GSVA, gene set variation analysis; GZMB, granzyme B; HMOX1, heme oxygenase 1; *Ido1*, indoleamine 2,3-dioxygenase 1; iDTR, inducible diphtheria toxin receptor; IFN-γ, interferon-gamma; IHC, immunohistochemistry; IVIS, in vivo imaging system; KYN, kynurenine; Luc, luciferase; Macro, macro-metastatic lung; MAFs, metastasis-associated fibroblasts; MEMα, minimum essential medium alpha; MFs, matrix fibroblasts; Micro, micro-metastatic lung; MxIF, multiplex immunofluorescence; MYH11, myosin heavy chain 11; MyoF1/2, myofibroblasts1/2; MyoFs, Myofibroblasts; N, normal lung; NRF2, nuclear factor erythroid 2-related factor 2; PBS, phosphate buffered saline; PD-1, programmed cell death protein-1; PDGFRA, platelet-derived growth factor receptor alpha; *PD-L1*, programmed cell death 1-ligand 1; PE, phycoerythrin; Pre, pre-metastatic lung; *Ptgs2*, prostaglandin-endoperoxide synthase 2; RSL3, (1S,3R)-2-(2-Chloroacetyl)-2,3,4,9-tetrahydro-1-[4-(methoxycarbonyl)phenyl]-1H-pyrido[3,4-b]indole-3-carboxylic acid methyl ester; scRNA-seq, single-cell RNA sequencing; shFTH1, short hairpin RNA of FTH1; shNC, negative control short hairpin RNA; TDO2/*Tdo2*, tryptophan 2,3-dioxygenase; UMAP, dimensional reduction analysis of uniform manifold approximation and projection; VDAC2, voltage dependent anion channel 2.

Yongcan Liu and Shanchun Chen contributed equally to this work.

Funding information
National Key Projects of Ministry of Science and Technology of China, Grant/Award Number: MOST2018YFE0113700; National Natural Science Foundation of China, Grant/Award Numbers: NSFC81874199, NSFC82173155; the Outstanding Professorship Program of Chongqing Medical University, Grant/Award Number: 2019-R10005; the Outstanding Postgraduate Fund of Chongqing Medical University, Grant/Award Numbers: BJRC202021, BJRC202025; the Chongqing Graduate Research and Innovation Project of the Chongqing Education Committee, Grant/Award Number: CYB22218

organotropic metastasis is poorly characterized. Here, we aimed to decipher the heterogeneity of MAFs and elucidate the distinct roles of these fibroblasts in pulmonary metastasis formation in breast cancer.

Methods: Mouse models of breast cancer pulmonary metastasis were established using an in vivo selection method of repeated injections of metastatic cells purified from the mouse lung. Single-cell RNA-sequencing (scRNA-seq) was employed to investigate the heterogeneity of MAFs. Transgenic mice were used to examine the contribution of tryptophan 2,3-dioxygenase-positive matrix fibroblasts ($TDO2^+$ MFs) in lung metastasis.

Results: We uncovered 3 subtypes of MAFs in the lung metastatic microenvironment, and their transcriptome profiles changed dynamically as lung metastasis evolved. As the predominant subtype, MFs were exclusively marked by platelet-derived growth factor receptor alpha (PDGFRA) and mainly located on the edge of the metastasis, and T cells were enriched around MFs. Notably, high MF signatures were significantly associated with poor survival in breast cancer patients. Lung metastases were markedly diminished, and the suppression of T cells was dramatically attenuated in MF-depleted experimental metastatic mouse models. We found that $TDO2^+$ MFs controlled pulmonary metastasis by producing kynurenine (KYN), which upregulated ferritin heavy chain 1 (FTH1) level in disseminated tumor cells (DTCs), enabling DTCs to resist ferroptosis. Moreover, $TDO2^+$ MF-secreted chemokines C-C motif chemokine ligand 8 (CCL8) and C-C motif chemokine ligand 11 (CCL11) recruited T cells. $TDO2^+$ MF-derived KYN induced T cell dysfunction. Conditional knockout of *Tdo2* in MFs diminished lung metastasis and enhanced immune activation.

Conclusions: Our study reveals crucial roles of $TDO2^+$ MFs in promoting lung metastasis and DTCs' immune evasion in the metastatic niche. It suggests that targeting the metabolism of lung-specific stromal cells may be an effective treatment strategy for breast cancer patients with lung metastasis.

KEYWORDS
Matrix fibroblasts, Lung metastasis, Tryptophan 2,3-dioxygenase, T cell dysfunction, Ferroptosis

1 | BACKGROUND

Metastasis is responsible for the majority of cancer deaths [1]. Many solid tumor types and subtypes, including breast cancer, display a non-random distribution of metastasis to distant organs, which is known as organotropism [2]. This phenomenon has long attracted extensive interest for oncologists. Lung is one of the most common sites of breast cancer metastasis, yet our understanding of the fundamental processes remains inadequate [3].

Among the steps involved in metastasis, colonization is considered the most challenging for disseminated tumor cells (DTCs) [4]. Unlike primary mammary or subcutaneous cancers, DTCs will face many obstacles in the lung, such as higher oxidative stress and ferroptosis threat [5, 6]. Thus, the support of the lung metastatic microenvironment is indispensable [7]. As the most abundant cell type in the tumor stroma, the role of metastasis-associated fibroblasts (MAFs) has become a new focus [8–11]. However, few previous studies have considered the heterogeneity of fibroblasts when studying the interactions between MAFs and DTCs or the immune-regulatory effect of MAFs. Recently, a metastasis-promoting lung fibroblast population with high prostaglandin-endoperoxide synthase 2 (*Ptgs2*) expression, named $Ptgs2^{hi}$ fibroblasts, was identified in breast cancer, which remodels the local immune

microenvironment and facilitates pre-metastatic niche formation [12]. However, no study to date has examined how lung fibroblast subtypes and their function changes over time with metastasis progression. Moreover, the underlying mechanisms by which MAF subsets help DTCs adapt to high stress environments need further clarification.

Here, we aimed to characterize the heterogeneity of MAFs and elucidate roles of specific subtype in favoring lung metastasis formation, which may offer valuable understandings into the mechanisms underlying metastatic progression and serve as useful targets when developing future therapies against metastatic disease.

2 | MATERIALS AND METHODS

2.1 | Cell culture

Murine mammary carcinoma cell 4T1 (American Type Culture Collection, Manassas, VA, USA) and E0771 (CH3 Biosystems, Amherst, NY, USA) were cultured in RPMI 1640 medium (Gibco, Grand Island, NY, USA) supplemented with 10% fetal bovine serum (FBS; Gibco) and 1% streptomycin/penicillin (C0222, Beyotime, Shanghai, China). Possible mycoplasma contamination was routinely and regularly monitored. 4T1/E0771 cells were retrovirally infected with a firefly luciferase reporter (for bioluminescence tracking) and selected with puromycin (1 μg/mL, 540222, Sigma Aldrich, St. Louis, MO, USA) for 14 days, named Luc-4T1 and Luc-E0771. Luc-4T1/E0771-LM3 cells were retrovirally infected with a green fluorescent protein (GFP) reporter and selected by fluorescence-activated cell sorting (FACS), named Luc-GFP-4T1-LM3 and Luc-GFP-E0771-LM3. All the cell lines used in the present study were verified by short tandem repeat genotyping prior to the start of the experiments.

2.2 | Mice

All animal experiments were approved by the Ethics Committee of Chongqing Medical University and conducted according to the guidelines for the Care and Use of Laboratory Animals of Chongqing Medical University (2021084). Female BALB/c mice (6 weeks; injected with 4T1 cells) and C57BL/6 mice (6 weeks; injected with E0771 cells) were purchased from the laboratory animal center of Chongqing Medical University, which were housed in specific pathogen free environment. MMTV-PyMT mice were a kind gift from Prof. Suling Liu (Fudan University). *Pdgfra-cre* transgenic mice, inducible diphtheria toxin receptor (iDTR) transgenic mice and *Tdo2*$^{flox/flox}$ (*Tdo2*$^{fl/fl}$) mice were from Cyagen Bioscience (Suzhou, Jiangsu, China). Mice were euthanized via cervical dislocation, when weakness or body weight loss (70% of control littermates) was observed.

To establish organotropic metastasis models, Luc-4T1 cells (1×10^6) or Luc-E0771 cells (1×10^6) were suspended in Phosphate Buffered Saline (PBS, 100 μL) and subsequently orthotopically implanted into mice. Mice were anaesthetized and intraperitoneally injected with D-luciferin (150 mg/kg, MX4603-100MG, Maokangbio, Shanghai, China) to monitor metastasis by bioluminescence imaging (BLI) with the in vivo imaging system (IVIS) (Caliper Life Sciences, Hopkinton, Massachusetts, USA). Lungs with metastasis were dissociated by type I collagenase (SCR103, Sigma Aldrich), and inoculated to obtain DTCs. With repeated fat pad injection of DTCs, organotropic metastasis tumor cells (Luc-4T1-LM3 and Luc-E0771-LM3) were selected by three rounds of selection in vivo.

For depletion of PDGFRA$^+$ MFs, *Pdgfra-cre* mice and iDTR mice were crossed to generate *Pdgfra*-DTR knock-in mice. Thereafter, mice were intraperitoneally injected with 25 ng/g of diphtheria toxin (DT, D0564, Sigma-Aldrich) twice per week to generate C57BL/6 iDTR$^+$ mice. *Pdgfra-cre* mice were further crossed with *Tdo2*$^{fl/fl}$ mice for generating C57BL/6 *Tdo2*^{cKO} mice. The same method was used to obtain BALB/c iDTR$^+$ mice and BALB/c *Tdo2*^{cKO} mice. MMTV-PyMT mice were crossed with C57BL/6 *Tdo2*^{cKO} mice for generating MMTV-PyMT *Tdo2*^{cKO} mice.

To compare the metastasis burden in iDTR$^+$ and iDTR$^-$ mice (or *Tdo2*$^{fl/fl}$ and *Tdo2*^{cKO} mice), 4T1-LM3 or E0771-LM3 (1×10^6) cells were injected (via the tail vein) into mice. When *Tdo2*$^{fl/fl}$ mice showed signs of weakness, mice were anaesthetized and lungs were imaged ex vivo by IVIS. Lung metastasis burden of MMTV-PyMT *Tdo2*^{cKO} mice were assessed 5-6 weeks after primary tumor formation. To detect the role of TDO2 and KYN in resistance to ferroptosis, immune escape and metastasis formation of DTCs, 680C91 (TDO2 inhibitors, HY-108681, MedChem Express, Monmouth Junction, NJ, USA) was administrated intraperitoneally once a day at a concentration of 15mg/kg; KYN (HY-104026, MedChem Express) was administered intraperitoneally every other day at a dose of 100 mg/kg; liproxstatin-1 (CAS 950455-15-9, TargetMol, Shanghai, China) was administered intraperitoneally once per day at the dose of 20 mg/kg. Dosing was started from 3 days after inoculation and stopped when control mice showed signs of weakness or imminent death.

2.3 | Primary cell isolation

To isolate primary lung stromal fibroblasts, lungs were harvested from 4 stages (N stage: normal; Pre stage: 2

weeks after inoculation; Micro stage: 3 weeks after inoculation; Macro stage: 6 weeks after inoculation) and minced into small pieces, then cultured with Minimum Essential Medium alpha (MEMα, ThermoFisher, Waltham, MA, USA). Primary lung stromal fibroblasts from *Tdo2*$^{fl/fl}$ or *Tdo2*^{cKO} mice were isolated as mentioned above. All fibroblasts used in the experiments were less than 6 passages.

Splenic CD4$^+$ and CD8$^+$ T cells were isolated by MojoSort™ Mouse CD4 T (480006, Biolegend, San Diego, CA, USA) or MojoSort™ Mouse CD8 T (480008, Biolegend) Cell Isolation Kit, respectively.

2.4 | Lung fibroblasts (LFs) function assay

To assay the function of LFs in DTCs colonization, primary N-LFs (LFs from normal lung), Pre-LFs (LFs from pre-metastatic lung), Micro-LFs (LFs from micro-metastatic lung) and Macro-LFs (LFs from macro-metastatic lung) were isolated and co-injected with 4T1-LM3 or E0771-LM3 cells in a 1:5 ratio (1×10^4 LFs and 5×10^4 tumor cells) via the tail vein, respectively. After 14 days, mice were euthanized (as described in Section 2.2) and lung tissues were collected. To assay the function of LFs in DTCs metastasis formation, 4T1-LM3 or E0771-LM3 (5×10^5) cells were orthotopically implanted into mice. After 10 days, N-LFs, Pre-LFs, Micro-LFs, and Macro-LFs (1×10^5) were administered through the tail vein. Mice were euthanized (as described in Section 2.2) on day 30. Lung tissues were collected and immediately stained with Bouin's fixative solution (PH0976, Phygene Scientific, Fuzhou, Fujian Province, China), counting lung nodules directly. Subsequently, the lungs were gently washed with running water and transferred to 70% ethanol to remove the fixative solution and used for further paraffin embedding.

2.5 | Conditioned medium (CM) and collagen contraction assay

To acquire tumor cell-/MF-derived CM, sorted tumor cells/MFs were inoculated in FBS-free 1640/ MEMα medium (37°C, 36 h). Then the supernatant was centrifuged (2,000×g, 4°C, 5 min) and filtered (0.22 μm filter), saved as CM.

Lung stromal fibroblasts (2×10^5) were suspended in 100 μL medium, which was mixed with 100 μL of Collagen Type I Rat Tail (containing 68.75 μL medium; Corning, NY, USA). The mixture was added to 1 well of 24-well plates in triplicate. After solidification, CM was added and incubated for 24 h, the gels were photographed. Image J (https://imagej.net/software/fiji/downloads) evaluated gel contraction.

2.6 | Single-cell RNA sequencing (scRNA-seq)

Lung samples (from N, Pre, Micro and Macro stages) were washed with Dulbecco's phosphate-buffered saline (DPBS, BL1109A, Biosharp, Hefei, Anhui, China) containing 10% streptomycin/penicillin and dissociated using a Tumor Dissociation Kit (130-096-730, Miltenyi Biotec, Bergisch Gladbach, Germany). Single cell suspensions were then filtered by a 70 μm (BS-70-CS, Biosharp) and a 40 μm cell filter (BS-40-CS, Biosharp) subsequently, lysed with Red Cell Lysis Solution (Biosharp), and washed with DPBS with 2% FBS. Hematopoietic (CD45$^+$), epithelial (CD326$^+$), endothelial (CD31$^+$) and tumor cells (GFP$^+$) were excluded by FACS to enrich CD326$^-$CD45$^-$CD31$^-$GFP$^-$ populations (fibroblast-enriched cells). Subsequently, fibroblast-enriched cells were used for scRNA-seq, and scRNA-seq profiles were generated by 10× Genomics sequencing.

With the GemCode Technology, single cells were encapsulated into nanoliter-sized GEMs (Gel Bead in emulsion). Post reverse transcription-GEMs were cleaned up, and cDNA was amplified. cDNA was fragmented with repaired fragments end, and the adaptors were ligated to fragments which were double sided solid-phase reversible immobilization (SPRI) selected. Another double sided SPRI selecting was carried out after sample index PCR (reaction volume: 100 μL; temperature and time: 98°C, 45 s; 98°C, 20 s; 54°C, 30 s, 11 cycles; 72°C, 20 s; 72°C, 1 min; 4°C). After checking fragments size distribution and quantifing the library, scRNA-seq was performed using the MGISEQ 2000 platform (BGI, Shenzhen, Guangdong, China).

2.7 | scRNA-seq data analysis

Raw scRNA-seq data needed map to the mouse reference genome (GRCm38) using the Cell Ranger Single Cell Software Suite (https://support.10xgenomics.com /single-cell-gene-expression/software/downloads/latest). R package Seurat (v 3.1.0) was used for next analysis. Cells with poor quality (expressing less than 200 genes, containing >90% of the maximum genes and >15% mitochondrial genes) were discarded. In total, 42,348 cells were obtained and assigned to 23 clusters. Copy number variation (CNV) analysis can find the contamination of malignant cells. Raw gene counts were normalized and the most highly variable genes were identified. Two-dimensional visualization was displayed by dimensional reduction analysis of uniform manifold approximation and projection (UMAP). The top differential genes were identified by FindConservedMarkers and served as marker genes (log fold change [logFC] > 0.25 and minimum per-

cent > 0.25). Then, cell type annotation was carried out according to Cell Marker database (http://biocc.hrbmu.edu.cn/CellMarker/). R package Monocle2 was utilized for Pseudotime trajectory analysis. Intercellular interaction analysis was done using CellPhoneDB (https://github.com/ventolab/cellphonedb-data). Gene set variation analysis (GSVA) was performed by R (v 1.40.1). Gene Ontology (GO) and Kyoto Encyclopedia of Genes and Genomes (KEGG) analysis of scRNA seq were performed on the Dr. Tom analysis system (BGI).

2.8 | Bulk RNA sequencing

Total RNA extracted from the tissues/cells was qualified using a Nano Drop and Agilent 2100 bioanalyzer (Termo Fisher Scientifc, Waltham, MA, USA). Subsequent RNA sequencing was carried out by BGI. Differentially expressed genes (DEGs) were selected based on $|\log_2 FC| > 2$. All subsequent analyses (unless noted) were performed on the Dr. Tom analysis system.

2.9 | Clinical tissue specimens

Lung metastasis specimens of breast cancer patients (5 cases) were from the First Affiliated Hospital of Chongqing Medical University (Chongqing, China). The specimens were obtained from previous clinical diagnosis by biopsy. All patients were informed and consented, which was approved by the Ethics Committee of Chongqing Medical University (2021084). The clinical information of all patients is listed in Supplementary Table S1.

2.10 | Clinical parameter analysis

Gene expression profiles of breast cancer patients (GSE14020, GSE14018, GSE209998 and GSE5327) were normalized using R v.4.3.1. For analysis of the relationship between MFs gene expression signatures and overall survival (time from diagnosis to death) as well as other clinical parameters (metastasis survival [time from lung metastasis to death] and lung metastasis-free survival [time from diagnosis to lung metastasis]), we stratified patients from GSE209998, GSE14020 and GSE14018 based on MFs signatures expression (log2 [FPKM_Value + 1]), using the median as cut-off. For analysis of the relationship between the *TDO2* level and lung metastasis-free survival, we stratified patients of GSE5327 based on *TDO2* expression, using the median as cut-off. Sangerbox 3.0 (http://sangerbox.com/home.html) was used for Pearson correlation analysis. Gene set enrichment analysis (GSEA, v4.3.2) in GSE14020 and GSE14018 was used to analyze the association between *TDO2* expression and lipid peroxisomal metabolism in each group. All analyses (unless noted) were performed using R (v.4.3.1).

2.11 | Flow cytometry

To profile LFs along metastatic stages, lungs were collected from mice (orthotopic injection of cancer cells) at weeks 2 (Pre), weeks 3 (Micro) and weeks 6 (Macro). The collected lungs were used to prepare single cell suspension. CD16/32 (101302, Biolegend) was added into cells (1×10^6) and incubated on ice (10 min). Next, the respective antibodies were added and incubated on ice (30 min). Cells were then washed and re-suspended in FACS buffer (2% FBS in DPBS), adding 4',6-diamidino-2-phenylindole (DAPI) (3 μg/mL, 422801, Biolegend). LFs were analyzed and sorted by FACS using two positive selection markers, CD140a and CD140b, and negative selection markers (CD326, CD45 and CD31). Briefly, $CD326^-CD45^-CD31^-CD140a^+/CD140b^+$ cells were regarded as fibroblasts. Numbers of LFs were counted by multiplying the total cells of lung with fibroblasts percentage. FlowJo V10 was used in data analysis (https://www.flowjo.com/).

To verify the dynamic shift in MAFs composition along metastatic stages, lungs were collected from mice at 2 weeks (Pre), 3 weeks (Micro) and 6 weeks (Macro) after orthotopic injection of cancer cells. After excluding hematopoietic ($CD45^+$), epithelial ($CD326^+$), endothelial ($CD31^+$) and tumor cells (GFP^+), the remaining cell population was regarded as the fibroblast-enriched cells. Subsequently, CD140b was used to identify fibroblasts; CD140a and CD146 were used to identify MFs and Myofibroblasts-2 (MyoF2) respectively, while the $CD140b^+CD140a^-CD146^-$ cells were regarded as Myofibroblasts-1 (MyoF1).

To elucidate the immune suppressive function of $Tdo2^{high}$ MFs, T cell function was analyzed. The isolated $CD4^+$ T and $CD8^+$ T cells were co-cultured with $Tdo2^{fl/fl}$-MFs, $Tdo2^{cKO}$-MFs with or without KYN (0.1 mmol/L) treatment. The system was also supplemented with anti-CD3 (250 ng/mL, 100238, Biolegend)/anti-CD28 antibodies (250 ng/mL, 102116, Biolegend) and interleukin-2 (IL-2, 10 ng/mL, 575404, Biolegend). Flow cytometry analyses of T cells was performed after 48 h. For in vivo analysis, single cell suspensions of lungs from $Tdo2^{fl/fl}$ and $Tdo2^{cKO}$ mice were prepared. Surface marker was stained for 0.5 h on ice. For intracellular cytokine staining, fixed cells were permeabilized with Cyto-Fast™ Fix/Perm Buffer Set (426803, Biolegend). For intra-nuclear staining, cells were permeabilized with True-Nuclear™ Transcription Factor Buffer Set (424401, Biolegend), and then respective anti-

bodies were added. Flow cytometry was performed using the BD FACSCanto™ plus machines (BD, Franklin Lakes, NJ, USA) and analyzed using FlowJo V10. The following antibodies were used in the study: phycoerythrin (PE) anti-mouse CD45 (2.5 ng/μL,103106, Biolegend), PE anti-mouse CD31 (10 ng/μL, 102408, Biolegend), PE anti-mouse CD326 (10 ng/μL, 118206, Biolegend), allophycocyanine (APC) anti-mouse CD140a (10 ng/μL, 135908, Biolegend), Brilliant Violet 421™anti-mouse CD140a (5 ng/μL, 135923, Biolegend), APC anti-mouse CD140b (10 ng/μL, 136008, Biolegend), PE/Cyanine7 anti-mouse CD146 (2.5 ng/μL, 134714, Biolegend), APC anti-mouse CD3 (5 ng/μL, 100236, Biolegend), fluoresceine isothiocyanate (FITC) anti-mouse CD4 (2.5 ng/μL, 100405, Biolegend), PE anti-mouse CD4 (2.5 ng/μL, 100512, Biolegend), FITC anti-mouse CD8 (10 ng/μL, 100706, Biolegend), PE anti-mouse CD8 (2.5 ng/μL, 100707, Biolegend), Brilliant Violet 421™anti-mouse FOXP3 (5 ng/μL, 126419, Biolegend), FITC anti-human/mouse granzyme B (GZMB, 5 μL per million cells in 100 μL staining volume, 396404, Biolegend), PE anti-mouse CD366 (Tim-3, 2.5 ng/μL, 119703, Biolegend), PE anti-mouse programmed cell death protein-1 (PD-1, 10 ng/μL, 135205, Biolegend).

2.12 | Hematoxylin-eosin (H&E) staining and immunohistochemistry (IHC)

The paraffin-embedded lungs were sectioned, deparaffinized and rehydrated. The slices were stained with H&E staining kit (Solarbio Life Sciences, Beijing, China). For IHC, after antigen retrieval, the sections were incubated with primary antibodies Ki67 (1:100, AF02778, Aifang Biotechnology, Changsha, Hunan, China), PTGS2 (1:100, SC56-06, HUABIO, Hangzhou, Zhejiang, China), TDO2 (1:100, 15880-1-AP, Proteintech, Wuhan, Hubei, China), fibronectin (FN, 1:300, 66042-1-Ig, Proteintech), periostin (POSTN, 1:4000, 66491-1-Ig, Proteintech) or alpha smooth muscle actin (α-SMA, 1:300, GB111364-100, Servicebio, Wuhan, Hubei, China), indoleamine-2,3-dioxygenase 1 (IDO1, 1:100, 13268-1-AP, Proteintech), ferritin heavy chain 1 (FTH1, 1:200, ET1610-78, HUABIO) overnight at 4°C. Subsequently, secondary antibody was incubated for 60 min. Stained with diaminobenizidine for 3 min, the slices finally stained with hematoxylin. The slices were scanned by 3DHISTECH Pannoramic MIDI or KFBIO KF-FL-020. Score IHC staining as follows: 0, no staining; 1, weak; 2, moderate; 3, strong. Score the percentage of stained cells as follows: 0, no staining; 1, < 10%; 2, 10-50%; and 3, > 50%. The IHC score was calculated by multiplying the staining score with the percentage score.

2.13 | Picrosirius red staining

To show the collagen fiber in macro-metastatic lung tissues, the de-paraffinized tissue sections at 4 μm thickness were stain with Modified Sirius Red Stain Kit (G1473-100ml, Solarbio Life Sciences) according to the manufacturers' instructions. Briefly, the tissue sections were stained with Iron Hematoxylin Staining Solution for 5-10 min, and washed with distilled water and tap water for 10-20 s and 5-10 min, respectively. Subsequently, Sirius Red Staining Solution was used for drip dyeing for 5-10 min. Thereafter, the slices were rinsed slightly with running water, and then dehydrated by series of ethanol and transparent by xylene, finally sealed with neutral gum and observed by optical microscope (Nikon, Tokyo, Japan).

2.14 | Multiplex immunofluorescence (MxIF)

For MxIF staining, the slices were stained with a 4-color Fluorescence kit (Aifang Biotechnology). Lung sections were de-paraffinized, rehydrated and permeabilized, followed by 15 min of citric acid antigen retrieval under high temperature and high pressure (100°C, 70-80 kPa). After natural cooling, the slides were blocked and incubated with primary antibodies for 17 h (4°C), and secondary antibodies and Opal TSA dyes for 50 min (25°C) and 10 min (25°C), respectively. The next rounds of staining consisted of antigen retrieval (15 min, 100°C), primary antibodies (16 h, 4°C), secondary antibodies (50min, 25°C), and Opal TSA dyes (10 min, 25°C). Afterwards, the slices were stained with DAPI (G1012, Servicebio) and finally sealed. The following antibodies were used: rabbit anti-mouse/human myosin-11 (MYH11, 1:50, 21404-1-AP, Proteintech), rabbit anti-mouse/human PDGFRA (1:200, ab203491, Abcam), rabbit anti-mouse/human TDO2 (1:200, 15880-1-AP, Proteintech), rabbit anti-mouse/human CD4 (1:50, ab288724, Abcam, Cambridge, MA, USA), rabbit anti-mouse/human CD8 (1:100, ab237709, Abcam), goat anti-rabbit polymer-horseradish peroxidase (HRP) secondary antibody (Aifang Biotechnology). The fluorescence signal was captured by 3DHISTECH Pannoramic MIDI II or KFBIO KF-FL-020. Image analysis of the MxIF was assessed by 2 certified pathologists.

2.15 | Cell counting kit-8 (CCK-8) assay

Erastin (HY-15763, MedChem Express) and (1S,3R)-2-(2-chloroacetyl)-2,3,4,9-tetrahydro-1-[4-(methoxycarbonyl) phenyl]-1H-pyrido[3,4-b]indole-3-carboxylic acid methyl

ester (RSL3, HY-100218A, MedChem Express) were used to induce ferroptosis in tumor cells. 4T1-LM3 (5,000 cells per well) and E0771-LM3 (1×10^4 cells per well) were added in 96-well plates (treated with erastin at concentrations of 0, 0.1, 0.5, 1, 2, 5 μmol/L or RSL3 at concentrations of 0, 0.2, 0.3, 0.5, 1, 2 μmol/L), with/without CM/KYN (0.1 mmol/L)/liproxstatin-1(1 μmol/L) treatment for 48 h. For determination of cell viability, CCK-8 (MRC-C23009-500T, Miracle, Chengdu, Sichuan, China) solution was added and cultured 2 h. Optical density (OD) at 450 nm was measured using an Eon microplate reader (BioTek, Biotek Winooski, Vermont, USA).

2.16 | qRT-PCR

The extracted RNA was reverse-transcribed into cDNA using PrimeScript RT Reagents Kit (RR036A, Takara). Gene expression was detected using TB Green™ Premix Ex Taq™ II (RR820A, Takara), and *β-Actin* was the internal control. PCR conditions: 30 s at 95°C for the preliminary denaturation, and 39 cycles of 5 s at 95°C, 30 s at 58°C, 20 s at 72°C for the amplification, and 10 min at 72°C for the extension. Primer sequences used are shown in Supplementary Table S2.

2.17 | Western blotting assay

The proteins were extracted by RIPA lysates (R0010, Solarbio Life Sciences) and quantified by BCA kit (P0010S, Beyotime). Then, proteins were transferred onto PVDF membrane and blocked for 60 min. PVDF membranes were co-incubated with primary antibody (FTH1, 1:2000, ET1610-78, HUABIO) overnight at 4°C. Washed with PBS, the membranes were incubated with appropriate HRP-conjugated secondary antibodies (Biosharp) for 60 min at 25°C, and the ECL kit (1705061, Bio-Rad, Hercules, CA, USA) was used to visualized proteins. After visualization, Image J software was used to quantify the gray value representing the protein expression levels.

2.18 | Establishment of stable expression cell lines

shFTH1 and control shRNA were synthesized by GenePharma (Shanghai, China) and cloned into PGLVH1/GFP vector. The sequences of shRNA were listed in Supplementary Table S3. Luc-4T1/E0771-LM3 cells were infected by the packaged lentivirus and selected by FACS to establish stable expression cells.

2.19 | Reactive oxygen species (ROS) detection

For ROS detection, 4T1-LM3/E0771-LM3 cells were incubated with BODIPY-C11 (2 μmol/L, thermo.D3861, Invitrogen, Carlsbad, CA, USA) for 30 min (37°C), trypsinized and washed, then analyzed by flow cytometer. For GFP-labeled tumor cells, erastin (1 μmol/L)/deferoxamine mesylate (DFOM, 100 μmol/L, S5742, Selleck, Shanghai, China)-treated 4T1-LM3/E0771-LM3 cells were incubated with Dihydroethidium (DHE, 2 μmol/L, S0063, Beyotime) for 30 min at 37°C, and other steps were consistent with BODIPY-C11.

2.20 | Determination of intracellular free Fe^{2+}

For Fe^{2+} determination, cells were seeded in 48-well plates and incubated with ferro-orange (F374, DOJINDO, Kumamoto, Japan). The cell nuclei were stained by Hoechst 33342 (IH0070, Solarbio Life Sciences). Images were captured by Leica DMi8 microscope (Leica microsystems, Wetzlar, Germany).

2.21 | High performance liquid chromatography (HPLC)

To measure KYN concentrations, cells were homogenized with RIPA lysis buffer, and total protein was quantified as mentioned above. The culture medium was centrifuged and filtered. Medium or cell lysis (100 μL) was mixed with 12% perchloric acid (100 μL) and vortex and centrifuged (10,000×g, 5 min, 4°C). The protein-free supernatants were determined by HPLC assay as described in previous studies [13].

2.22 | High content real-time imaging

$CD140a^+$ MFs freshly isolated by flow cytometry were incubated (3,000 cells per microplate) in 96-well microplates (CellCarrier-96 Ultra, PerkinElmer, Waltham, MA, USA) and cultured for 6 h. $CD3^+$ T cells were sorted from spleen by MojoSort™ Mouse CD3 Selection Kit (480100, Biolegend) and subsequently incubated with carboxyfluorescein diacetate succinimidyl ester (CFSE, C34570, Invitrogen), then $CD3^+$ T cells were added to the (10,000 cells per well) microplates and followed by incubation in a high-content imaging system (Operetta CLS, PerkinElmer), and images were acquired every 0.5h for 8 h.

2.23 | Enzyme-linked immunosorbent assay (ELISA) analysis

To detect IFN-γ from $CD4^+$ T or $CD8^+$ T cells, the collected supernatants were centrifuged (2,000×g, 4°C, 5 min) and filtered. The levels of IFN-γ were measured using a mouse IFN-γ ELISA Kit (EMC101g.96, NeoBioscience, Shenzhen Guangdong, China).

2.24 | Statistics

Statistical analysis was performed by GraphPad 8.0.2 software (https://www.graphpad.com). Experiments were repeated at least three times. Comparisons between two groups were performed using a two-tailed Student's t-test, and multiple groups were compared using a one-way ANOVA. Pearson correlation analysis was employed to identify the correlation between variables. Statistical significance was defined as $^*P < 0.05$; $^{**}P < 0.01$; $^{***}P < 0.001$.

3 | RESULTS

3.1 | Activated lung fibroblasts promoted lung metastasis of breast cancer

Stromal fibroblasts are the major cells in the lung microenvironment [14]. It has been reported that parental cells (human triple-negative breast cancer MDA-MB-231 cells) and their highly metastatic cancer cells (MDA-MB-231-LM2) have similar functions to induce LF activation, but MDA-MB-231-LM2 cells function earlier and more strongly [9].

To better explore roles of local LFs in breast cancer lung metastasis, we generated lung-tropic metastasis derivatives 4T1/E0771-LM3 by repeated fat pad injection and metastatic clone selection, using luciferase-labeled murine breast cancer cell lines 4T1 and E0771 (Supplementary Figure S1A). The metastatic ability and incidence of lung-tropic metastasis increased with the number of selection and expansion rounds, confirmed by BLI (Supplementary Figure S1B-C). Compared with CM from parental cells, LFs stimulated with CM from LM3 cells showed a significant increase in collagen gel contraction (Supplementary Figure S1D).

Metastatic progression in mice could be divided into three stages: Pre, Micro (when lungs harbor DTCs to form primary micro-metastases) and Macro stages (when macro-metastases are prominent and widespread) [9, 15]. Extracellular matrix (ECM) remodeling is a hallmark of the metastatic niche [16], as demonstrated by elevated FN, POSTN expression and picrosirius red staining in both 4T1-LM3 model (Figure 1A-B) and E0771-LM3 model (Supplementary Figure S2A-B). Fibroblasts are the major players in ECM production [17]. Enhanced expression of α-SMA (a marker of activated fibroblasts) (Figure 1A, Supplementary Figure S2A) suggested the activation of LFs during metastasis progression [9]. Sorted by FACS using two positive selection markers, CD140a (PDGFRA) and CD140b (PDGFRB), and a group of negative selection markers (GFP, CD326, CD45 and CD31) (Supplementary Figure S2C), activated LFs were found to be obviously increased accompanying metastasis progression (Figure 1C). Next, we isolated normal and activated LFs from the lungs of BALB/c and C57BL/6 mice at different stages, named N-LFs, Pre-LFs, Micro-LFs, Macro-LFs, respectively. To understand whether Pre-LFs, Micro-LFs and Macro-LFs had an effect on lung metastasis of breast cancer, DTC colonization and metastatic nodules were evaluated. After co-injection of 4T1-LM3 or E0771-LM3 cells with LFs via the tail vein, Pre-LFs, Micro-LFs and Macro-LFs strikingly promoted lung colonization of DTCs in comparison with N-LFs (Figure 1D, Supplementary Figure S2D). 4T1-LM3 or E0771-LM3 cells were injected into mice mammary gland fat pad to generate primary tumor, and LFs were administered through the tail vein. Injection of Pre-LFs, Micro-LFs and Macro-LFs clearly increased lung metastatic nodules to a greater extent than N-LFs (Figure 1E, Supplementary Figure S2E). Together, these data substantiated that lung stromal fibroblasts acquired metastasis-promoting property.

3.2 | Distinct fibroblast subtypes in breast cancer lung metastasis ecosystem

Recent studies reported that primary tumors harbor different fibroblast subtypes with diverse origins and functions [18, 19]; however, the roles of fibroblast subtypes need to be determined in the metastatic microenvironment. To identify fibroblast subtypes associated with breast cancer metastasis progression, we sampled LFs along time points of metastasis development (Pre, Micro and Macro stages) with the normal lung from naive mice as controls, generating scRNA-seq profiles by 10× Genomics sequencing (Figure 2A). We applied a negative selection gating strategy to exclude hematopoietic ($CD45^+$), epithelial ($CD326^+$), endothelial ($CD31^+$) and tumor cells (GFP^+). The remaining $CD326^-/CD45^-/CD31^-/GFP^-$ cell population was regarded as fibroblast-enriched cells and used for scRNA-seq analysis [20] (Supplementary Figure S3A). A total of 42,348 high-quality cells were retained (Figure 2B), which could be assigned to 23 clusters through Seurat analysis (Figure 2C). Thereafter, CNV analysis was

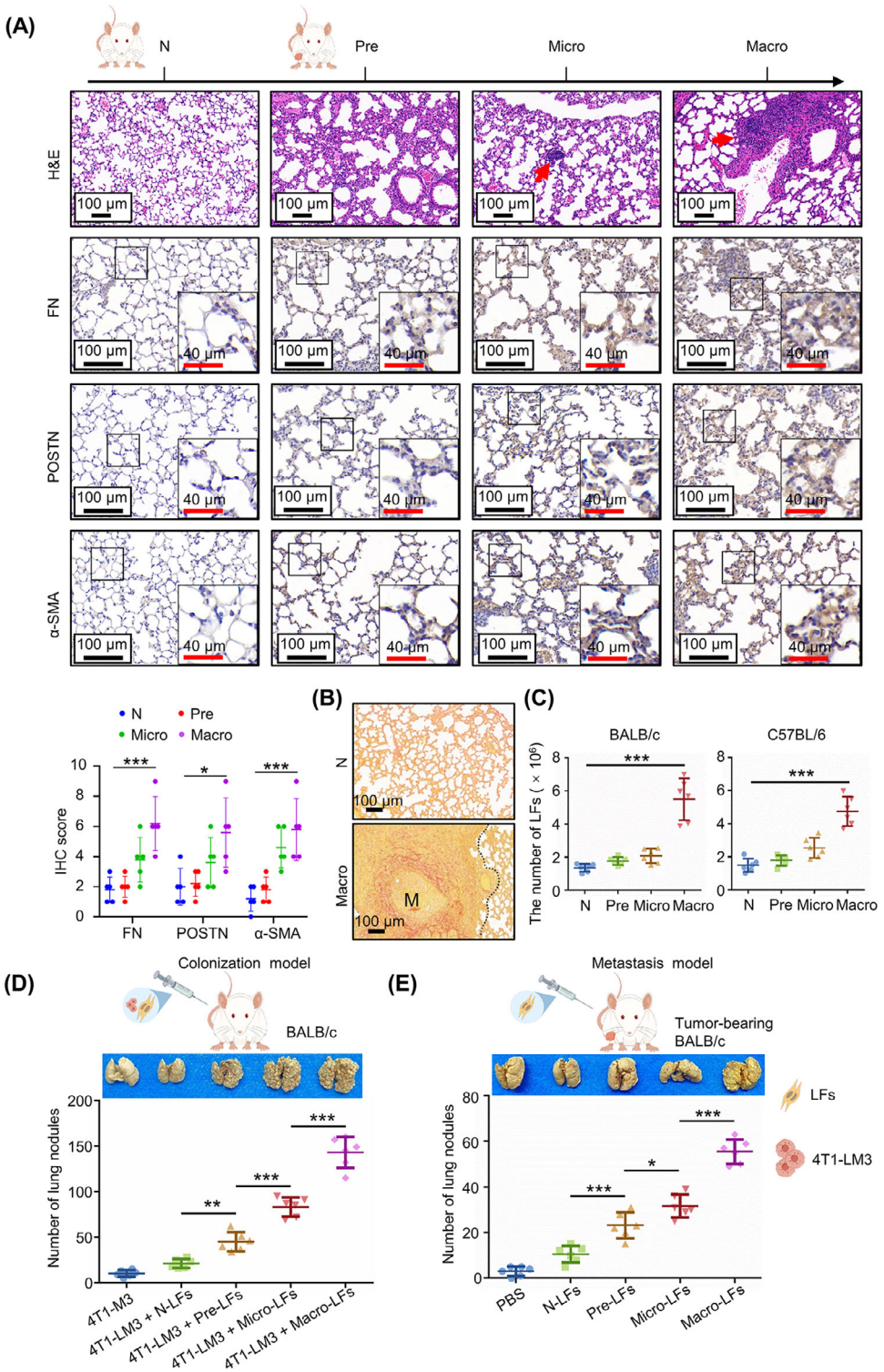

FIGURE 1 Activated lung fibroblasts promoted lung metastasis of breast cancer. (A) Representative images and quantification of H&E and IHC staining of histological lung sections from BALB/c mice ($n = 5$). The arrows indicate lung nodules. (B) Picrosirius red staining showing collagen fibers in lung tissues from BALB/c mice. (C) Quantification of LFs at indicated stage ($n = 6$). (D) Quantification of lung nodules ($n = 6$). 4T1-LM3 cells were mixed with N-, Pre-, Micro- or Macro-LFs (5×10^4 4T1-LM3 cells and 1×10^4 LFs), which were injected into BALB/c mice via the tail vein. After 14 days, lung nodules were counted. (E) Quantification of lung nodules ($n = 6$). 4T1-LM3 cells (5×10^5) were orthotopically implanted into BALB/c mice. After 10 days, NL-, Pre-, Micro- and Macro-LFs (1×10^5) were injected into tumor-bearing mice via the tail vein, respectively. Results represent mean ± SD. One-way ANOVA in A, C, D and E. $^*P < 0.05$; $^{**}P < 0.01$; $^{***}P < 0.001$. 4T1-LM3, 4T1-lung metastasis 3; α-SMA, alpha smooth muscle actin; FN, fibronectin 1; POSTN, periostin; H&E, hematoxylin & eosin; IHC, immunohistochemistry; LFs, lung fibroblasts; M, metastatic lesions; Macro, macro-metastatic lung; Micro, micro-metastatic lung; N, normal lung; PBS, phosphate buffered saline; Pre, pre-metastatic lung.

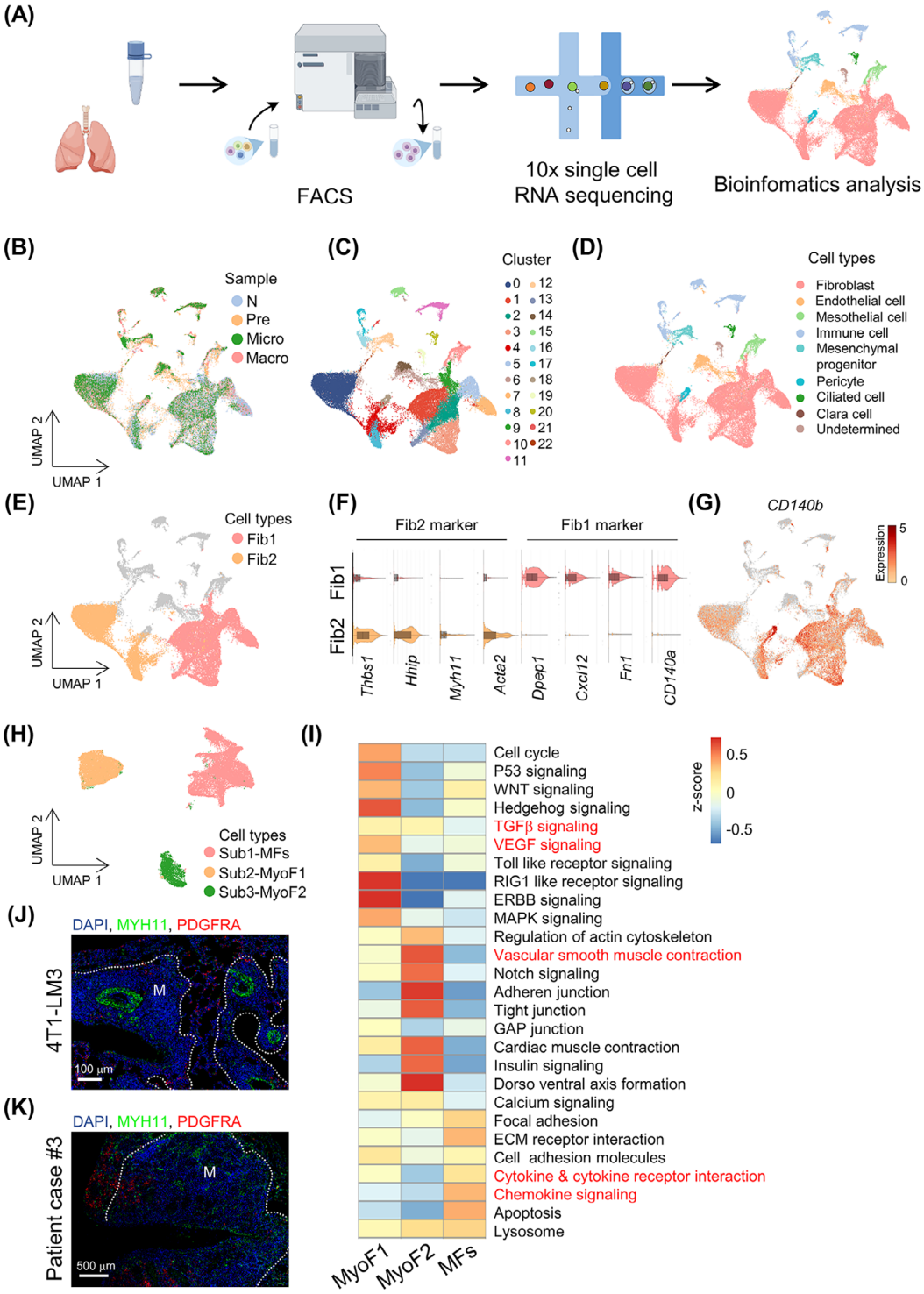

FIGURE 2 Distinct fibroblast subtypes in breast cancer lung metastasis ecosystem. (A) Workflow depicting experimental strategy of scRNA-seq for FACS-enriched fibroblasts. (B-D) UMAP plots indicating cell distribution (B), cell cluster (C) and cell type of samples (D). (E) UMAP plot showing two main fibroblast subtypes. (F) Violin plots exhibiting genes expression in fibroblast subtypes. (G) UMAP plot displaying *CD140b* expression. (H) UMAP plot manifesting 3 fibroblasts subtypes. (I) Pathway activity (scored by GSVA) in fibroblast subtypes. (J-K) Representative immunofluorescence images for PDGFRA, MYH11 and DAPI in lung tissues of BALB/c mice (J) and a breast cancer patient (K) with metastatic foci. Abbreviations: scRNA-seq, single-cell RNA sequencing; FACS, fluorescence-activated cell sorting; N, normal lung; Pre, pre-metastatic lung; Micro, micro-metastatic lung; Macro, macro-metastatic lung; UMAP, uniform manifold approximation and projection; 4T1-LM3, 4T1-lung metastasis 3; *CD140a/b*, platelet derived growth factor receptor alpha/beta; Fib1/2, fibroblast subtypes 1/2; *Thbs1*, thrombospondin 1; *Hhip*, hedgehog interacting protein; *Myh11*, myosin heavy chain 11; *Acta2*, actin alpha 2; *Dpep1*, dipeptidase 1; *Cxcl12*, C-X-C motif chemokine ligand 12; *Fn1*, fibronectin 1; GSVA, gene set variation analysis; MFs, matrix fibroblasts; MyoF1/2, myofibroblasts1/2; M: metastatic lesions; PDGFRA, platelet derived growth factor receptor alpha; DAPI, 4',6-diamidino-2-phenylindole.

employed to exclude the contamination of malignant cells (Supplementary Figure S3B). According to marker gene expression, clusters were identified as fibroblast, endothelial cell, mesothelial cell, immune cell, mesenchymal progenitor, pericyte, ciliated cell and clara cell (Figure 2D, Supplementary Figure S4A-B). Cluster 19 was not defined due to the lack of known marker gene expression and functional pathways, and was eliminated from further analysis.

Interestingly, fibroblasts could be obviously partitioned into two broad classes (Figure 2E-F): fibroblast 1 (Fib1, *CD140a*$^+$; 18,338 cells; clusters 1, 2, 3, 5, 7, 9, 13) and fibroblast 2 (Fib2, *Myh11*$^+$; 13,518 cells; clusters 0, 4, 8). Both fibroblast subtypes highly expressed canonical fibroblast markers such as *CD140b*, secreted protein acidic and rich in cysteine (*Sparc*) and vimentin (*Vim*) [17] (Figure 2G, Supplementary Figure S4C). However, fibroblast UMAP plot exhibited 3 re-clustered subtypes (Figure 2H). Each subtype of fibroblasts displayed distinct transcriptional profiles (Supplementary Figure S4D). Subtype 1 (corresponding to Fib1 in Figure 2E; named matrix fibroblasts [MFs, CD140a$^+$]) was characterized by high ECM signatures, including collagen molecules (collagen type V alpha 2 chain [*Col5a2*], collagen type VI alpha 3 chain [*Col6a3*]), fibronectin 1 (*Fn1*), lumican (*Lum*) and versican (*Vcan*), as well as inflammatory chemokines (C-X-C motif chemokine ligand 12 [*Cxcl12*], interleukin 6 [*Il6*], C-C motif chemokine ligand 7 [*Ccl7*], C-C motif chemokine ligand 2 [*Ccl2*]) and complement genes (complement C3 [*C3*] and complement C7 [*C7*]) (Figure 2F, Supplementary Figure S5A). Simultaneously, terms of GO and KEGG analysis enriched for MFs were related to ECM and collagen fibril organization, inflammatory response regulation and amino acid/cytokine response (Supplementary Figure S5B-C), suggesting that this subtype may participate in immune regulation. Subtypes 2 and 3 (corresponding to Fib2 in Figure 2E) mainly expressed known marker genes for myofibroblasts [21], including actin alpha 2 (*Acta2*), *Myh11*, transgelin (*Tagln*) and hedgehog interacting protein (*Hhip*) (Supplementary Figure S4D). Moreover, GSVA of Subtypes 2 and 3 showed significant enrichment for the transforming growth factor beta (TGFβ) signaling pathway, the vascular endothelial growth factor (VEGF) signaling pathway and vascular smooth muscle contraction (Figure 2I), indicating their microvascular signature. Accordingly, Subtypes 2 and 3 were named Myofibroblasts-1 (MyoF1) and Myofibroblasts-2 (MyoF2), respectively (Figure 2H). To validate the main fibroblast subtypes described above, MxIF staining was performed in lung sections (harboring 4T1-LM3 metastases), and PDGFRA and MYH11 could obviously distinguish MFs and MyoFs (Figure 2J). Notably, PDGFRA$^+$ fibroblasts were mainly localized in the invasive front of or around metastases; conversely, MYH11$^+$ fibroblasts were mainly localized in the tumor core and microvascular region. Furthermore, morphological differences between MFs and MyoFs (sorted by FACS) in the in vitro culture system were also observed: MFs were plump and irregular; MyoFs were long and spindly (Supplementary Figure S5D). To test the robustness of the fibroblast classification, we repeated the same MxIF staining in lung metastases paraffin sections of two other murine models (E0771-LM3 and MMTV-PyMT transgenic mice model) (Supplementary Figure S5E-F) and breast cancer patients (Figure 2K); classification and location of LFs were consistent with the 4T1-LM3 model, suggesting their conservative character of fibroblast heterogeneity. Together, these data demonstrated mutually exclusive, morphologically distinct fibroblast subtypes in the breast cancer lung metastasis ecosystem.

3.3 | Composition and transcriptional program of fibroblast subtypes were dynamically reshaped

Accumulating evidence indicates that the tumor microenvironment changes dynamically with tumor progression [22, 23]. Comparably, we hypothesized that lung stromal heterogeneity may become more complicated during tumor metastasis. As expected, each fibroblast population was reproducible across metastasis stages; however, fibroblast composition varied extensively at different time points. MFs accounted for the predominant population at any stage; the proportion of MyoF1 increased gradually, especially at the Micro stage; the abundance of MyoF2 increased at the Pre stage but decreased in subsequent stages (Figure 3A). The dynamic shift in fibroblast subtypes was clearly unveiled by FACS (Supplementary Figure S6A). To determine whether LFs phenotypically evolved as metastases progressed, we characterized transcriptional program changes of fibroblast subtypes with GSVA. Most pathways were shared but diverse degrees of activation in the Pre, Micro, and Macro stages were observed (Figure 3B). For example, chemokine signaling and inflammatory response signatures were observed in MFs since pre-metastases and were further enriched in macro-metastases (Figure 3B). Mobilization and recruitment of neutrophils in the pre-metastatic niche have been widely recognized [24]. Interestingly, we found that neutrophils were enriched around MFs at the Pre stage in multiple mice models (Figure 3C). Here, dynamic changes in gene expression (e.g., *C3*, *Cxcl12*) and transcription profile of MFs might provide a reasonable explanation. TGFβ, VEGF signaling and endocytoses were gradually enriched in MyoF1 and MyoF2 (Figure 3B). Consistently, MyoFs were abundant around endothelial cells (Sup-

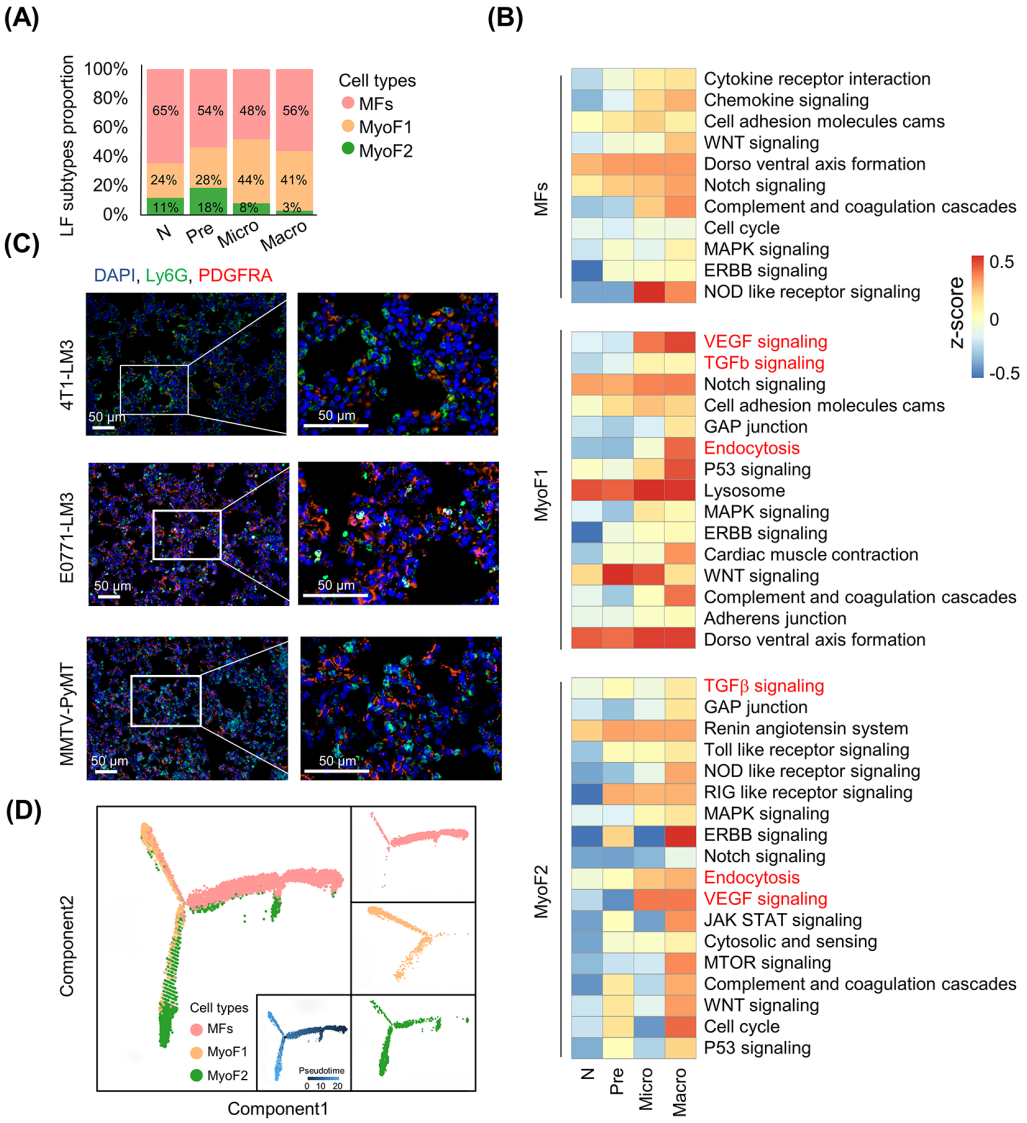

FIGURE 3 Composition and transcriptional program of fibroblast subtypes were dynamically reshaped. (A) The proportion of LF subtypes during metastasis evolution. (B) The activated signaling (scored per cell by GSVA) in LF subtypes during metastasis evolution. (C) Representative immunofluorescence images for DAPI/Ly6G/PDGFRA in lung tissues of BALB/c (inoculated with 4T1-LM3 cells), C57BL/6 (inoculated with E0771-LM3 cells) and MMTV-PyMT mice. (D) Pseudotime analysis of fibroblast subtypes. Abbreviations: LF, lung fibroblast; MFs, matrix fibroblasts; MyoF1/2, myofibroblasts1/2; N, normal lung; Pre, pre-metastatic lung; Micro, micro-metastatic lung; Macro, macro-metastatic lung; GSVA, gene set variation analysis; PDGFRA, platelet derived growth factor receptor alpha; DAPI, 4',6-diamidino-2-phenylindole; Ly6G, lymphocyte antigen 6 complex; 4T1-LM3, 4T1-lung metastasis 3; E0771-LM3, E0771-lung metastasis 3, MMTV-PyMT, mouse mammary tumor virus- polyoma middle T antigen.

plementary Figure S6B). To expand our findings, we analyzed metabolism-related biological changes in MAF subtypes. Compared with MyoFs, metabolic programs of MFs displayed stage-dependent characteristics. For instance, amino acid metabolism (e.g., tryptophan [Trp] metabolism) of MFs was instigated early in metastatic stage and functionally persisted throughout metastatic progression, while fatty acid metabolism was enriched since the Micro stage (Supplementary Figure S6C). These data revealed that fibroblast activation-related genes and signaling pathways were gradually enriched since the Pre stage to support tumor-promoting abilities of fibroblast subtypes. To explore whether there is mutual transformation among fibroblast subtypes, as previously reported [25], the Monocle2 algorithm was employed to observe the developmental trajectories of three subtypes. We found a clear tree structure beginning with MFs and ending with MyoF1 and MyoF2 (Figure 3D), suggesting an evolution from MFs towards MyoFs. Together, the composition and transcriptional program of fibroblast subtypes were dynamically reshaped and may contribute to lung-tropic metastasis.

3.4 | MF depletion decreased lung metastasis progress

The huge proportion of immune cells in lungs with manifest metastasis may hamper the capture of other cells in scRNA-seq (Supplementary Figure S7A). To avoid interference from abundant immune cells, we removed immune cells ($CD45^+$) by FACS and used the remnant cells from macro-metastatic lung tissue for scRNA-seq, yielding data that could better explore the interactions between DTCs and niche cells in the lung. After cell type identification (Supplementary Figure S7B-D), CellPhoneDB was used to examine intercellular interactions based on ligand-receptor pairs [20]. Interestingly, fibroblasts were the predominant cell population interacting with tumor cells, and among these, MFs had the most ligand-receptor interactions with DTCs (Figure 4A-B). Meanwhile, a high MF signature was associated with decreased cumulative survival in breast cancer patients with lung metastases (Figure 4C). Importantly, a high MF signature also revealed a strong trend toward worsened metastasis survival and lung metastasis-free survival in breast cancer patients with lung metastases (Supplementary Figure S7E).

Given the specific expression of PDGFRA in MFs, we explored the functions of MFs on lung metastasis formation using conditional knockout mice to selectively deplete $PDGFRA^+$ MFs. By crossing *Pdgfra-cre* transgenic mice with iDTR transgenic mice, we established conditionally depleted MFs in the lung (Supplementary Figure S7F). As expected, the deficiency in MFs was more than 85% following the administration of DT (Supplementary Figure S7G). Surprisingly, intravenous injection of 4T1-LM3 or E0771-LM3 exhibited notable reduction of DTC colonies in the lung of $iDTR^+$ mice compared with $iDTR^-$ mice (Figure 4D-E). Moreover, $iDTR^+$ mice had less metastasis burden and much longer survival than $iDTR^-$ littermates (Figure 4F-G). Simultaneously, dramatically decreased Ki-67 was detected in metastatic nodules of $iDTR^+$ mice in comparison with $iDTR^-$ mice (Figure 4H). Collectively, these data showed that selective ablation of $PDGFRA^+$ MFs led to a marked and sustained decrease in metastasis burden.

3.5 | TDO2 was highly expressed exclusively in MFs

The significant reduction in metastasis burden caused by $PDGFRA^+$ MF ablation led us to investigate how MFs contribute to DTC growth and metastasis formation in the lung. To address this question, bulk RNA-seq of purified fibroblast subtypes was carried out. Gene expression data displayed a high correlation ($R > 0.97$) between bulk and cognate single-cell profiles (Supplementary Figure S8A). We then tried to select all DEGs between metastatic MFs (M-MFs) and normal MFs (N-MFs) using the bulk RNA-seq data based on $|\log_2 FC| > 2$. Given the gradually activated transcriptional program in MFs in the metastasis process, we reasoned that the genes significantly upregulated in M-MFs (1,109 genes) and those with higher expression in M-MFs than in metastatic MyoFs (M-MyoFs) (420 genes) would be the viably pro-metastatic candidates (Supplementary Figure S8B). Notably, among the 420 genes, there were robust metabolism and cytokine-cytokine receptor interaction biology processes enriched in KEGG analysis of M-MFs (Figure 5A), which replicated the analysis of scRNA-seq data (Figure 3B, Supplementary Figure S6C). Among these signaling processes, Trp metabolism caught our attention, not only because it was instigated early and persisted during advanced metastatic disease (Supplementary Figure S6C) but also because that *Tdo2* (encoding tryptophan 2,3-dioxygenase, TDO2 [26]; a key enzyme in catalytic conversion of L-tryptophan [L-Trp] into kynurenine [KYN]) was one of the most upregulated genes in M-MFs (Figure 5B). Moreover, UMAP plot and qRT-PCR analysis showed that *Tdo2* was exclusively or highly expressed in MFs rather than in other cell types (e.g., epithelial cells, immune cells and endothelial cells) (Supplementary Figure S8C-D). Indeed, TDO2 was abundant in lungs harboring metastases compared with healthy lungs; more importantly, TDO2 was mainly expressed in the lung stroma but not metastatic nodules, which was similar to MFs' localization (Figure 5C); and DTCs in metastatic foci were TDO2-negative (Figure 5C). Similar results were obtained in the E0771-LM3 model (Supplementary Figure S8E). More interestingly, the predominant expression of TDO2 was in $PDGFRA^+$ MFs, but not in $MYH11^+$ MyoFs (Figure 5D, Supplementary Figure S8D); accordingly, $Tdo2^{high}$ MFs (M-MFs) produced more KYN than N-MFs (Supplementary Figure S8F). In addition, co-localization of TDO2 with PDGFRA was observed in lung metastatic tissues of breast cancer patients (Figure 5E). Conditional depletion of MFs in $iDTR^+$ mice notably decreased TDO2 levels in lung metastatic foci (Figure 5F). Previous research showed that tumor cells themselves could promote tumor progression by producing large amounts of KYN dependent on the Trp-IDO1 axis (IDO1, the other rate-limiting enzyme in Trp metabolism) [27]. IHC staining showed extremely low IDO1 expression in both primary and metastatic sites of mice and breast cancer patients (Supplementary Figure S8G). Accordingly, KYN production of tumor cells (primary tumor cells and DTCs) was significantly lower than that of MFs during the whole metastasis process (Supplementary Figure S8H). In short, TDO2 was exclusively expressed in MFs.

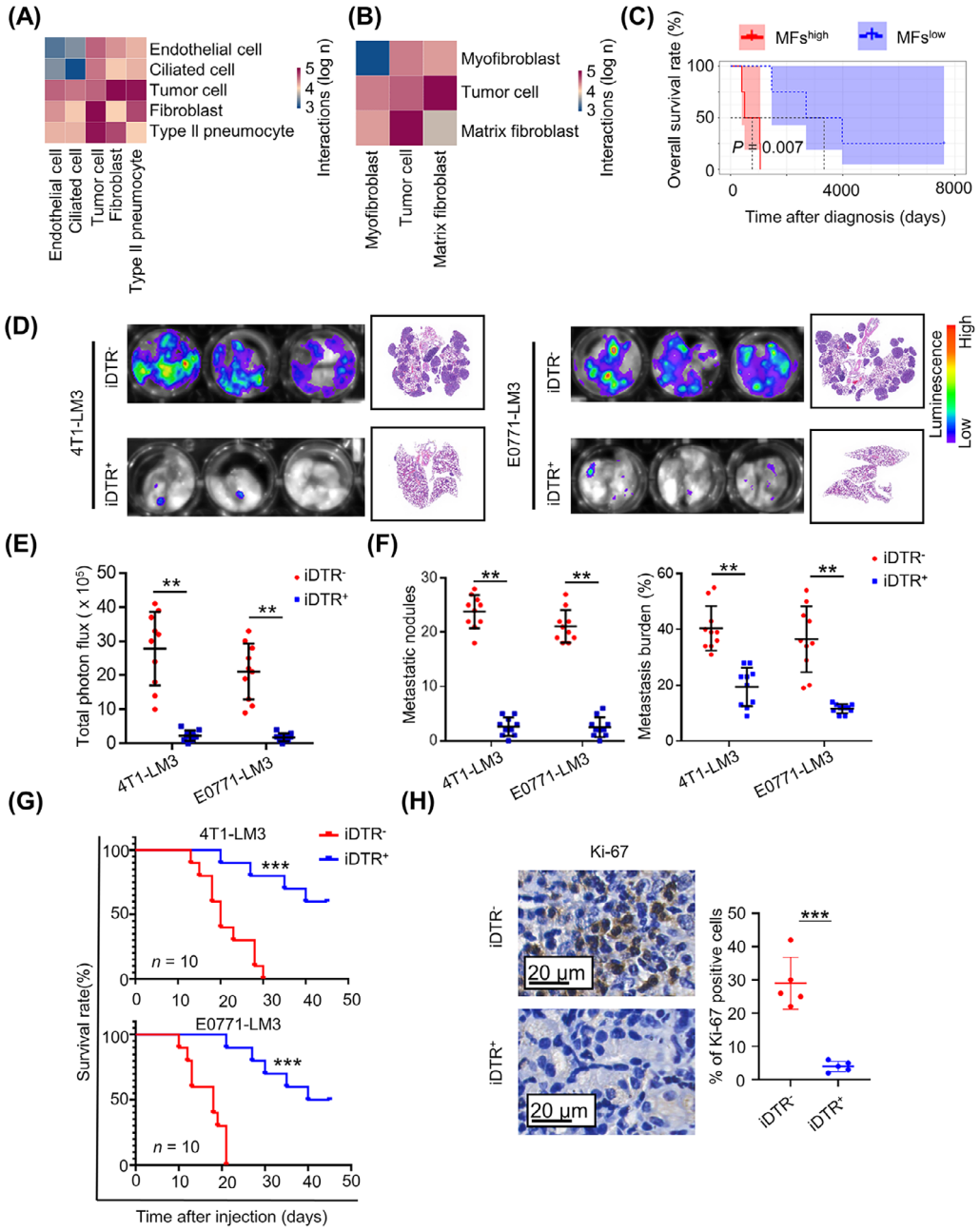

FIGURE 4 MFs depletion decreased lung metastasis progress. (A-B) CellPhoneDB analysis of all cell types in lung (A), or between MFs or MyoFs and tumor cells (B). (C) Overall survival in lung metastasis samples from breast cancer patients (GSE209998) with different MFs signature levels. (D-E) Representative bioluminescence imaging, H&E staining (D) and quantification of lung metastatic intensity (E) in iDTR$^+$ and iDTR$^-$ mice ($n = 10$). (F) Quantification of metastatic nodules and metastasis burden in iDTR$^+$ and iDTR$^-$ mice ($n = 10$). (G) Kaplan-Meier curve of iDTR$^+$ and iDTR$^-$ mice after 4T1-LM3 or E0771-LM3 cells injection ($n = 10$). (H) Ki-67 expression in lung metastatic foci of iDTR$^+$ and iDTR$^-$ mice ($n = 5$). Results represent mean ± SD. Log-rank test in C and G, student's t-test in E, F and H. $^{**}P < 0.01$; $^{***}P < 0.001$. Abbreviations: MFs, matrix fibroblasts; MyoFs, myofibroblasts; 4T1-LM3, 4T1-lung metastasis 3; E0771-LM3, E0771-lung metastasis 3; iDTR, inducible diphtheria toxin receptor; H&E, hematoxylin & eosin.

3.6 | *Tdo2*^{high} MFs fostered lung metastasis

The TDO enzyme is mainly expressed in the liver, whose activity balances the total amount of Trp in the body [28]. Trp enters the liver, where most is oxidized to acetoacetyl-coenzyme A and used for the synthesis of nicotinamide adenine dinucleotide. Extrahepatic organs that metabolize Trp along the KYN pathway (KP) contribute most to circulating levels of KYN and KP metabolites [29]. To determine the function of TDO2 in MFs, we crossed *Tdo2*$^{fl/fl}$ mice with *Pdgfra-Cre* mice to generate *Tdo2*^{cKO} mice, resulting

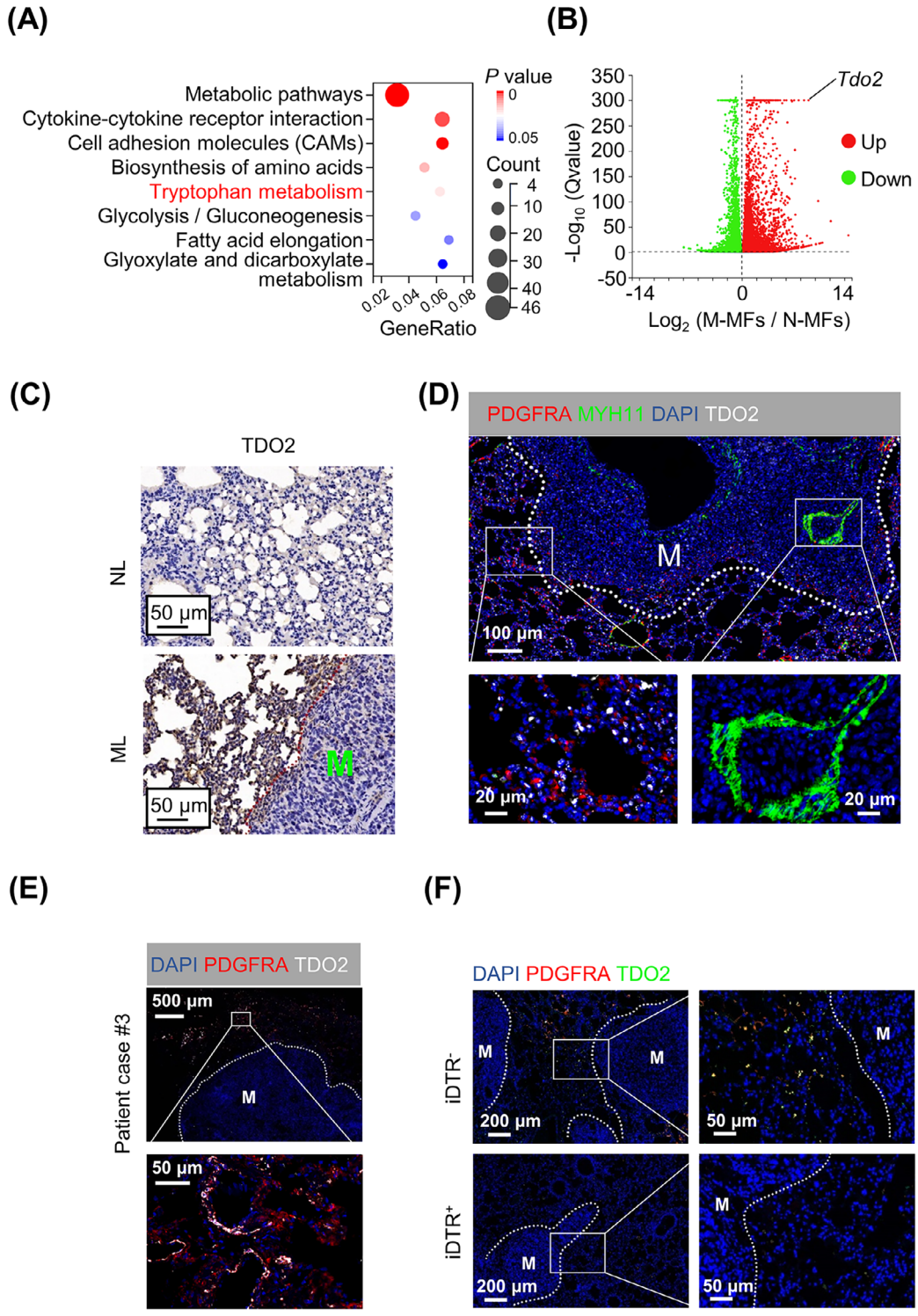

FIGURE 5 TDO2 was highly expressed exclusively in MFs. (A) KEGG analysis of M-MFs. (B) Volcano plot showing DEGs between MFs from normal (N-MFs) and metastatic lung (M-MFs). Red dots: up-regulated genes ($log_2FC > 0$, Q value < 0.05), green dots: down-regulated genes ($log_2FC < 0$, Q value < 0.05). (C) IHC images of TDO2 in normal and metastatic lung tissues of BALB/c mice. (D) MxIF staining for PDGFRA, MYH11, TDO2 and DAPI in metastatic lung tissue of BALB/c mice. (E-F) IF staining for PDGFRA, TDO2 and DAPI in metastatic lung tissue of patient (E) and iDTR$^+$ and iDTR$^-$ mice (F). Abbreviations: KEGG, Kyoto Encyclopedia of Genes and Genomes; DEGs, differentially expressed genes; M-MFs, MFs from metastatic lung; N-MFs, MFs from normal lung; NL, normal lung; ML, metastatic lung; IHC, immunohistochemistry; MxIF, multiplex immunofluorescence; PDGFRA, platelet derived growth factor receptor alpha; MYH11, myosin heavy chain 11; DAPI, 4',6-diamidino-2-phenylindole; *Tdo2*/TDO2, tryptophan 2,3-dioxygenase; iDTR, inducible diphtheria toxin receptor; M, metastatic lesions; IF, immunofluorescence.

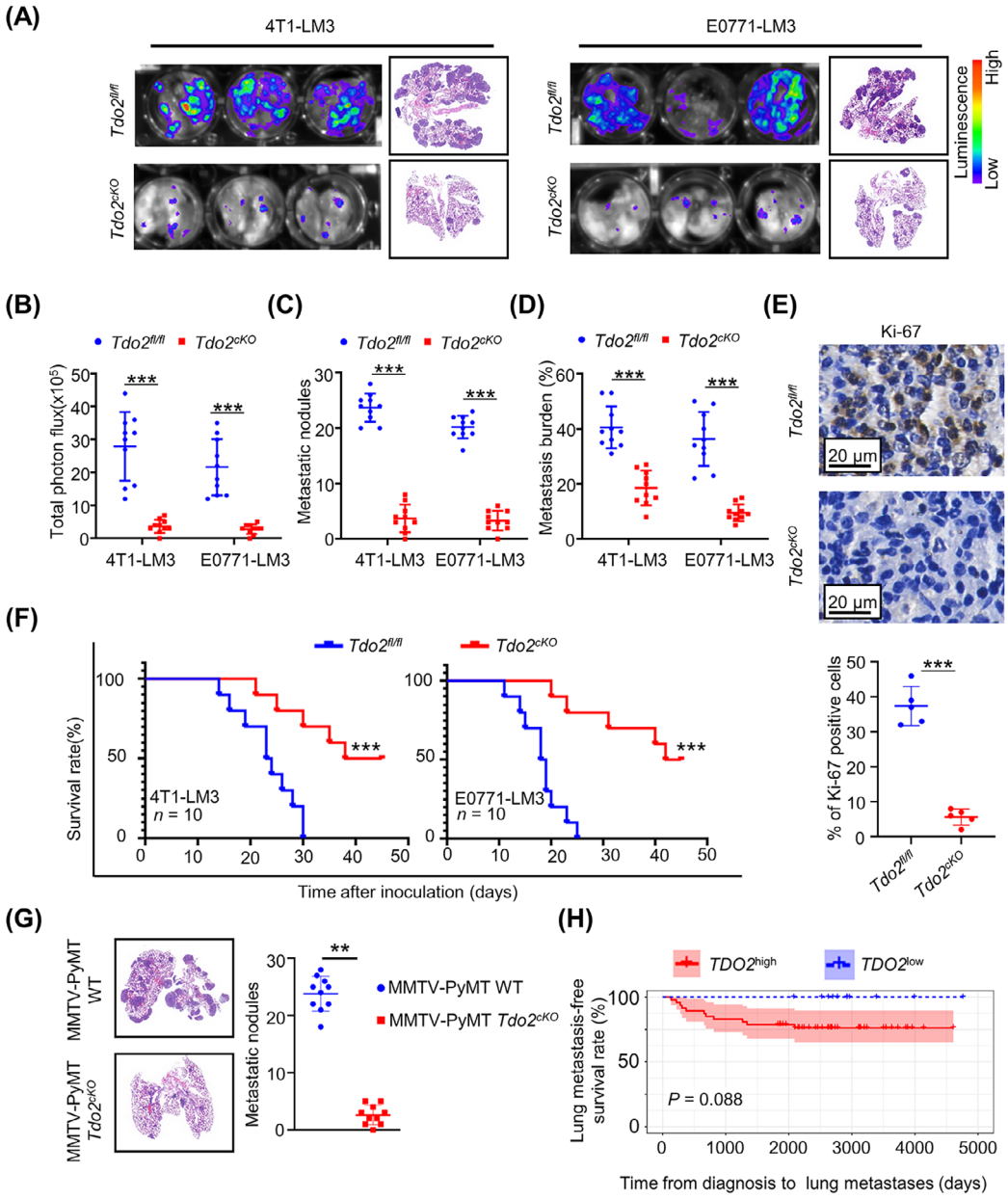

FIGURE 6 *Tdo2*^{high} MFs fostered lung metastasis. (A-B) Representative bioluminescence imaging, H&E images (A) and quantification (B) of lung metastasis in *Tdo2*$^{fl/fl}$ and *Tdo2*^{cKO} mice ($n = 10$). (C-D) Quantification of lung nodules (C) and metastasis burden (D) ($n = 10$). (E) IHC images and quantification of Ki-67 levels in *Tdo2*$^{fl/fl}$ and *Tdo2*^{cKO} mice. (F) Survival of *Tdo2*$^{fl/fl}$ and *Tdo2*^{cKO} mice ($n = 10$) after injection (via the tail vein) of 4T1-LM3 (left) or E0771-LM3 (right) cells. Kaplan-Meier test. (G) H&E images (left) and quantification of pulmonary nodules (right) in MMTV-PyMT *Tdo2*^{cKO} and WT mice ($n = 10$). (H) Lung metastasis-free survival in mammary carcinoma patients (GSE5327) with different *TDO2* levels. Results represent mean ± SD. Student's t-test in B, C, D, E, and G, log-rank test in F and H. $^{**}P < 0.01$; $^{***}P < 0.001$. Abbreviations: H&E, hematoxylin & eosin; 4T1-LM3, 4T1-lung metastasis 3; E0771-LM3, E0771-lung metastasis 3; IHC, immunohistochemistry; *Tdo2*$^{fl/fl}$, *Tdo2*$^{flox/flox}$; *Tdo2*^{cKO}, *Tdo2* conditioned knockout; WT, wild type; MMTV-PyMT, mouse mammary tumor virus- polyoma middle T antigen.

in > 95% reduction of *Tdo2* mRNA and TDO2 protein in MFs of lung tissue (Supplementary Figure S8I). Encouragingly, no apparent compensatory effect of indoleamine-2,3-dioxygenase 1 (*Ido1*, encoding IDO1) was observed (Supplementary Figure S8J); consistently, MFs isolated from *Tdo2*^{cKO} mice had minimal KYN production (Supplementary Figure S8K). In line with iDTR^{+} mice, *Tdo2* deficiency in *Pdgfra*$^{+}$ fibroblasts dramatically mitigated metastasis burden in both 4T1-LM3 and E0771-LM3 metastatic mice models (Figure 6A-D). Correspondingly, tumor cells from metastatic foci in *Tdo2*^{cKO} mice showed a significant reduction of cell proliferation (Figure 6E). Moreover, *Tdo2*^{cKO}

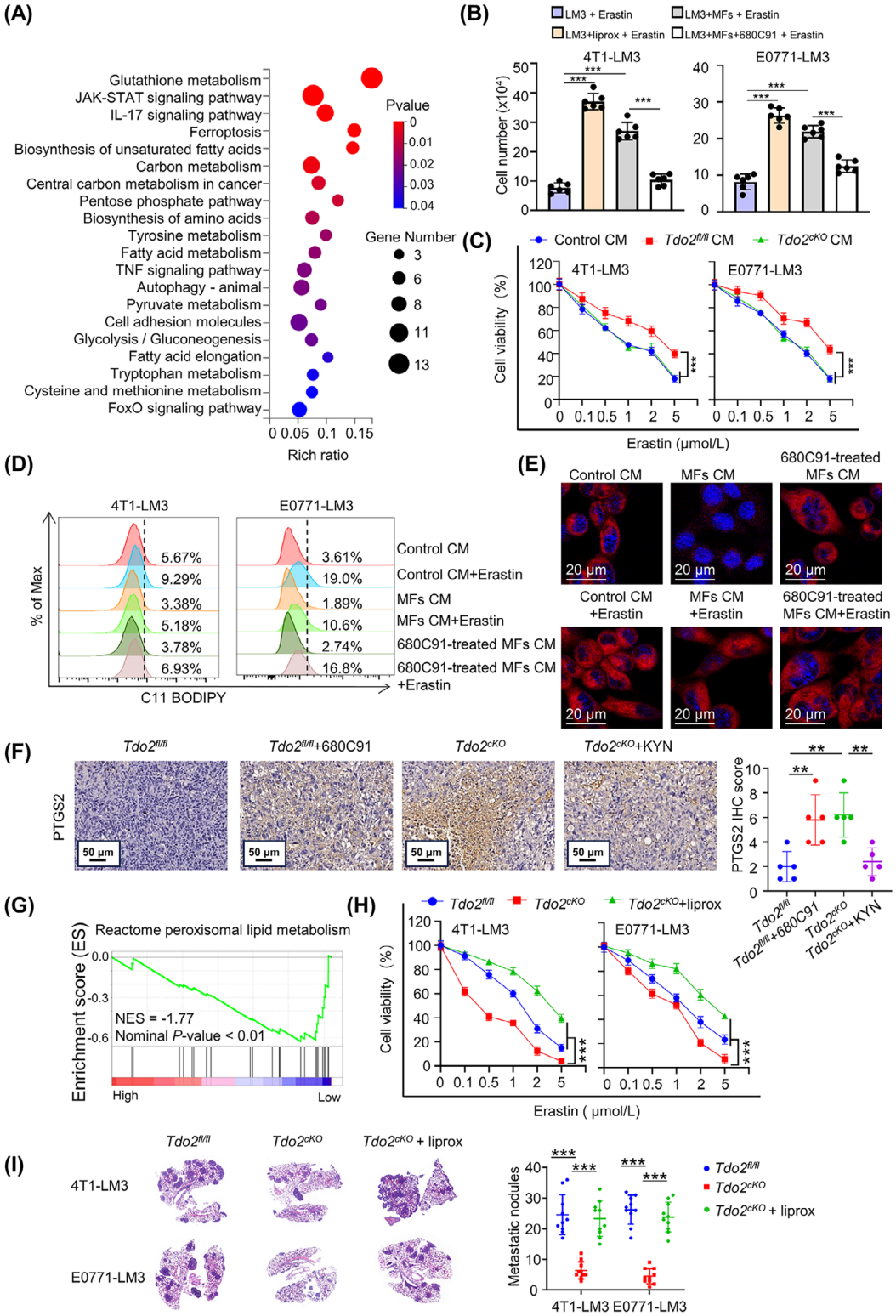

FIGURE 7 TDO2-KYN protected DTCs from ferroptosis. (A) KEGG analysis of 4T1-LM3 cells cultured with *Tdo2*^{high} MF-CM. (B) Cell viability of 4T1-LM3 and E0771-LM3 cells co-cultured with MFs and treated with 1 μmol/L erastin, 25 μmol/L 680C91, 1 μmol/L liproxstatin-1 in indicated groups. (C) Cell viability of tumor cells treated with an increasing concentration of erastin in indicated groups ($n = 6$). (D) Lipid ROS of tumor cells cultured with indicated CM for 2 days ± 25 μmol/L 680C91 and treated with 1 μmol/L erastin, respectively. (E) Representing fluorescent images indicating intracellular Fe^{2+} concentration in 4T1-LM3 cells cultured with indicated CM ± 25 μmol/L 680C91 and treated with 1 μmol/L erastin for 2 days. (F) IHC images and quantification of PTGS2 in pulmonary nodules from *Tdo2*$^{fl/fl}$ and *Tdo2*^{cKO} mice with indicated treatment ($n = 5$). (G) GSEA analysis of the enrichment of peroxisomal lipid metabolism in pulmonary metastasis samples from mammary carcinoma patients (GSE14020 and GSE14018) with different *TDO2* levels. (H) Cell viability of 4T1-LM3 and

lung metastasis-burdened mice had much longer survival than *Tdo2*$^{fl/fl}$ littermates (Figure 6F). However, the growth of primary tumors was not significantly different between *Tdo2*$^{fl/fl}$ and *Tdo2*^{cKO} mice (Supplementary Figure S8L-M). *Tdo2* deficiency dramatically reduced the lung metastatic burden of parental cells (4T1 and E0771) while there was no significant change in liver, bone, and brain metastatic burden (Supplementary Figure S8N), which indicated that the MF-TDO2 axis was specific in the lung. To better recapitulate the role of *Tdo2*^{high} MFs in lung metastasis of patients with breast cancer, we crossed the *Tdo2*^{cKO} strain with MMTV-PyMT mice, evaluating the effects of MF-specific *Tdo2* deficiency on spontaneous lung metastasis in this model. Consistent with the aforementioned findings, deletion of *Tdo2* in MFs significantly reduced spontaneous lung metastases in MMTV-PyMT mice (Figure 6G). Furthermore, we also observed a trend toward worsened lung metastasis-free survival in breast cancer patients with higher *TDO2* expression (Figure 6H). These data demonstrated that TDO2-dependent MF program promoted lung metastasis formation.

3.7 | TDO2-KYN protected DTCs from ferroptosis

To further understand how *Tdo2*^{high} MFs affect the fate of DTCs, we performed unbiased RNA sequencing in *Tdo2*^{high} MF-CM-treated 4T1-LM3 cells. Using KEGG analysis, metabolic pathways and ferroptosis were markedly enriched in *Tdo2*^{high} MF-CM-treated DTCs (Figure 7A). The lung metastasis microenvironment exhibits higher ferroptotic stress compared to primary mammary cancers [30]; thus, developing resistance to ferroptosis is necessary for DTCs. It is reported that aberrant amino acid metabolism played crucial roles in ferroptosis. In particular, the Trp metabolite KYN could protect tumor cells from ferroptosis and promote tumor growth [31]. We therefore wondered whether *Tdo2*^{high} MFs could decrease the sensitivity of DTCs to ferroptosis. TDO2 and ferroptosis suppressors (nuclear factor erythroid 2-related factor 2 [NRF2] and heme oxygenase 1 [HMOX1]) expression levels showed positive correlations in lung metastases of breast cancer patients; consistently, TDO2 and ferroptosis driver (voltage dependent anion channel 2 [VDAC2]) levels presented a negative correlation (Supplementary Figure S9). Interestingly, the positive correlations between TDO2 and ferroptosis suppressors FTH1 and aldo-keto reductase family 1 member C1 (AKR1C1) were also replicated in lung metastases of osteosarcoma patients (Supplementary Figure S9A). Liproxstatin-1 treatment, a ferroptosis antagonist, reduced erastin-induced DTC death. DTCs, co-cultured with *Tdo2*^{high} MFs, developed resistance to erastin-induced ferroptosis, whereas 680C91 (a TDO2 inhibitor) treatment significantly ameliorated DTCs' ferroptosis resistance (Figure 7B). Consistently, CM from *Tdo2*^{cKO} MFs failed to protect tumor cells against erastin- or RSL3-induced cell death in comparison with CM from *Tdo2*$^{fl/fl}$ littermates (Figure 7C, Supplementary Figure S10A). These data suggested that *Tdo2*^{high} MFs played an important role in protecting DTCs from ferroptosis. Ferroptosis is an iron-dependent form of regulated cell death, characterized by altered iron homeostasis, reduced defense against oxidative stress, and abnormal lipid peroxidation [32]. Checked by BODIPY-C11 staining, DTCs cultured with *Tdo2*^{high} MF-CM had lower lipid ROS levels, while 680C91 treatment increased lipid ROS of DTCs (Figure 7D). Besides, accumulation of lipid ROS induced by erastin was decreased in DTCs cultured with *Tdo2*^{high} MF-CM rather than in DTCs cultured with 680C91-treated *Tdo2*^{high} MF-CM (Figure 7D). Remarkably lower cellular Fe^{2+} was detected in DTCs cultured with *Tdo2*^{high} MF-CM; besides, *Tdo2*^{high} MF-CM could rescue the erastin-induced augmentation of Fe^{2+}, while CM from 680C91-treated *Tdo2*^{high} MFs failed to maintain low cellular Fe^{2+} level (Figure 7E, Supplementary Figure S10B).

Recent reports showed that KYN-derived metabolites activated anti-ferroptotic pathways [31]. KYN can be converted to anthranilic acid by kynureninase (KYNU) and to kynurenic acid by kynurenine aminotransferases (kynurenine aminotransferase 1 [*Kyat1*, KATI], aminoadipate aminotransferase [*Aadat*, KATII], kynurenine aminotransferase 3 [*Kyat3*, KATIII]). Kynurenine monooxygenase (KMO) controls the conversion of KYN to neuroactive and neurotoxic KP metabolites, including quinolinic acid [29]. To distinguish the forms in which KYN functioned in our study, we examined kynurenine aminotransferase expression in both *Tdo2*^{high} MFs and

E0771-LM3 cells co-cultured with MFs from *Tdo2*$^{fl/fl}$ mice and *Tdo2*^{cKO} mice in the presence or absence of 1 μmol/L liproxstatin-1 and supplemented with an increasing concentration of erastin for 2 days ($n = 6$). (I) H&E images (left) and quantification of pulmonary nodules (right) in *Tdo2*$^{fl/fl}$ mice and *Tdo2*^{cKO} mice (with/without liproxstatin-1 supplement, $n = 10$). Results represent mean ± SD. Two-way ANOVA test in C and H, one-way ANOVA in B, F and I. $^{**}P < 0.01$; $^{***}P < 0.001$. Abbreviations: KEGG, Kyoto Encyclopedia of Genes and Genomes; 4T1-LM3, 4T1-lung metastasis 3; E0771-LM3, E0771-lung metastasis 3; MFs, matrix fibroblasts; CM, conditioned medium; PTGS2, prostaglandin-endoperoxide synthase 2; IHC, immunohistochemistry; KYN, kynurenine; liprox, liproxstatin-1; *Tdo2*$^{fl/fl}$, *Tdo2*$^{flox/flox}$; *Tdo2*^{cKO}, *Tdo2* conditioned knockout; WT, wild type; GSVA, gene set variation analysis; H&E, hematoxylin & eosin.

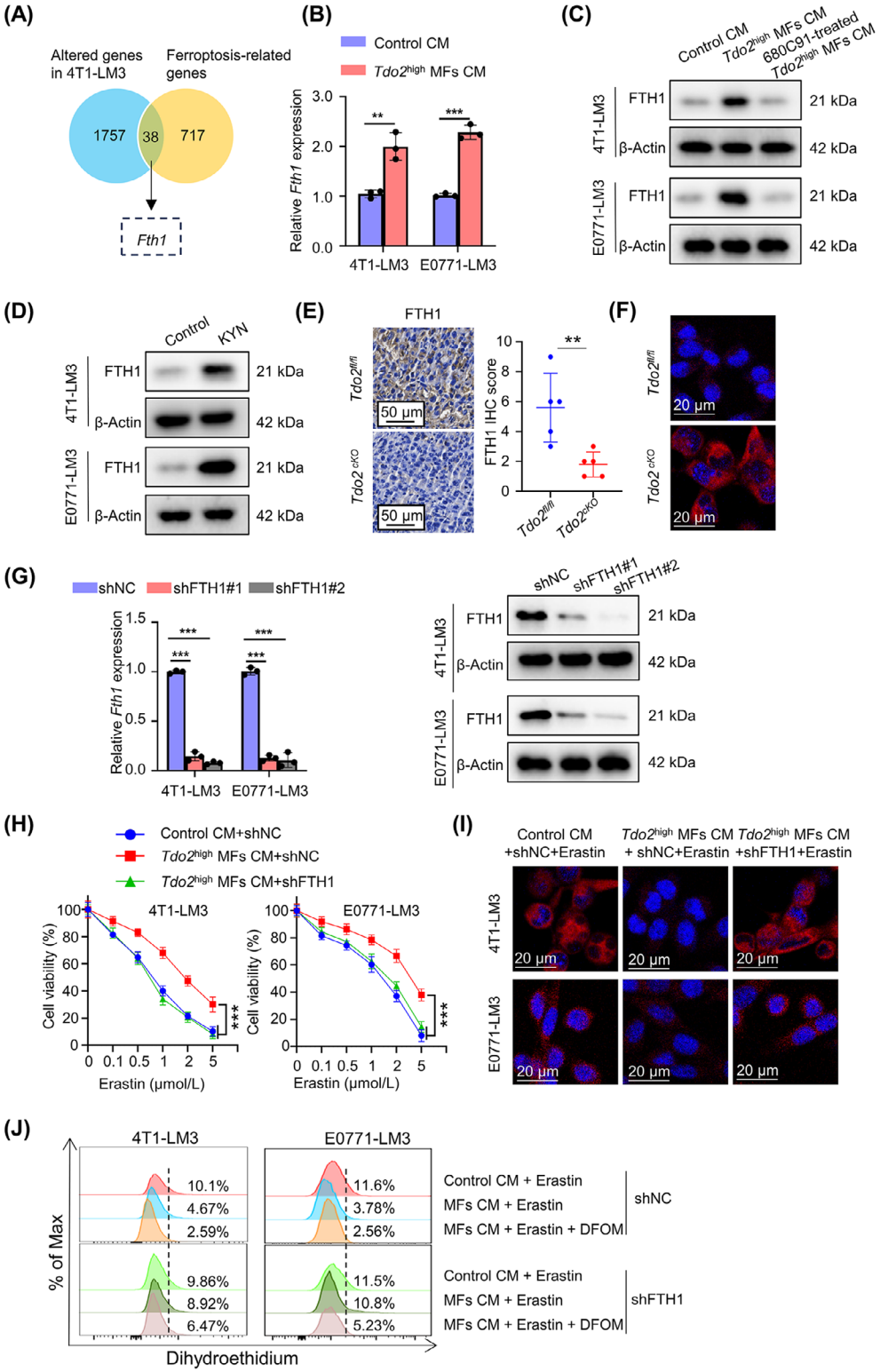

FIGURE 8 KYN upregulated FTH1 level in DTCs, enabling DTCs to resist ferroptosis. (A) Venn diagram displaying the significantly changed ferroptosis related genes in 4T1-LM3 cells. (B) qRT-PCR analysis showing *Fth1* expression in 4T1-LM3 and E0771-LM3 cells treated with indicated CM ($n = 3$). (C) Western blotting showing FTH1 expression in the indicated groups. (D) Western blotting showing FTH1 level in 4T1-LM3 and E0771-LM3 cells treated with or without KYN (200 μmol/L) for 48 h. (E) IHC images and quantification of FTH1 in lung metastases derived from $Tdo2^{fl/fl}$ and $Tdo2^{cKO}$ mice ($n = 5$). (F) Representing fluorescent images indicating intracellular Fe^{2+} concentration in DTCs from Figure 8E. (G) Western blotting and qPCR analysis showing FTH1 expression in 4T1-LM3 and E0771-LM3 cells transfected with negative control or FTH1 shRNA ($n = 3$). (H) Cell viability of 4T1-LM3-shFTH1/E0771-LM3-shFTH1 and control cells cultured with the indicated CM and supplemented with an increasing concentration of erastin for 2 days ($n = 6$). (I) Representative fluorescent images

DTCs (4T1-LM4 and E0771-LM4 cells). However, low gene expression of KATI–KATIII was observed in both *Tdo2*^{high} MFs and DTCs (Supplementary Figure S10C). In addition, *Tdo2*^{high} MFs and DTCs also showed extremely low *Kynu* and *Kmo* expression in scRNA-seq (Supplementary Figure S10D). Therefore, directly treating DTCs with KYN, which also markedly elevated resistance to erastin- or RSL3-induced ferroptosis, decreased lipid peroxidation and cellular Fe^{2+} level as *Tdo2*^{high} MF-CM done (Supplementary Figure S10E-H).

We next assessed TDO2-KYN-modulated DTC ferroptosis resistance in vivo. Firstly, we checked the levels of PTGS2 [33], a ferroptosis downstream marker, in lung metastases from *Tdo2*^{cKO} mice and *Tdo2*$^{fl/fl}$ littermates. There was higher PTGS2 expression in the lung metastases from *Tdo2*^{cKO} mice than *Tdo2*$^{fl/fl}$ mice; treatment with KYN remarkably decreased PTGS2 in *Tdo2*^{cKO} mice. Conversely, treating *Tdo2*$^{fl/fl}$ mice with 680C91 dramatically increased PTGS2 levels in lung metastases (Figure 7F). More importantly, in breast cancer patients, lung metastases with higher *TDO2* had fewer lipid peroxisomal metabolism-associated genes (Figure 7G), which supported the above findings in mice. To determine whether TDO2-KYN-modulated ferroptosis contributed to metastatic outgrowth, DTCs were co-cultured with *Tdo2*^{cKO} MFs, then treated with liproxstatin-1. DTCs in *Tdo2*^{cKO} MF co-culture system were more sensitive to erastin compared with DTCs in *Tdo2*$^{fl/fl}$ MF co-culture system; however, liproxstatin-1 supplement to DTCs and *Tdo2*^{cKO} MFs co-culture system attenuated erastin-induced ferroptosis (Figure 7H). *Tdo2* depletion-induced decrease in metastases (Figure 7I) and corresponding Ki-67-positive tumor cell ratio (Supplementary Figure S10I), and increase of PTGS2 levels in the lung metastases of *Tdo2*^{cKO} mice (Supplementary Figure S10J) were all effectually blunted by liproxstatin-1 supplement. These findings suggested an essential role of TDO2-KYN in protecting DTCs against ferroptosis to foster lung metastasis.

To define the mechanism by which *Tdo2*^{high} MF-secreted KYN protects DTCs from ferroptosis, the transcriptome of 4T1-LM3 cells treated with CM from M-MFs or N-MFs were analyzed, and the DEGs involved in ferroptosis were determined (Figure 8A). *Fth1* was one of the most upregulated genes in M-MF-CM-treated 4T1-LM3 cells, which was confirmed by qRT-PCR (Figure 8B). The enhanced FTH1 protein was further confirmed in 4T1/E0771-LM3 cells co-cultured with CM from *Tdo2*^{high} MFs, while 680C91-treated *Tdo2*^{high} MF-CM failed to elevate the FTH1 protein level (Figure 8C). We further demonstrated that KYN could stimulate FTH1 expression by supplementing KYN in the medium (Figure 8D). Besides, FTH1 level in lung metastases was lower in *Tdo2*^{cKO} mice than in *Tdo2*$^{fl/fl}$ mice (Figure 8E). Correspondingly, more free Fe^{2+} accumulated in DTCs derived from *Tdo2*^{cKO} mice in comparison with *Tdo2*$^{fl/fl}$ mice (Figure 8F).

FTH1, heavy chains of ferritin, is an iron storage protein, which combines and stores ferric irons, thus limiting the generation of destructive redox species [34]. Excess ferrous ions (Fe^{2+}) generate abundant toxic ROS through the Fenton reaction [35]. To ascertain whether FTH1 was required for DTCs' ferroptosis resistance mediated by *Tdo2*^{high} MFs, FTH1 was knocked down by shRNA in 4T1-LM3 and E0771-LM3 cells, respectively (Figure 8G). CM from *Tdo2*^{high} MFs could protect 4T1/E0771-LM3 cells, but not FTH1-depleted 4T1/E0771-LM3 cells, against erastin-induced cell death (Figure 8H). The intracellular accumulation of Fe^{2+} was accordingly decreased in the parental 4T1/E0771-LM3 cells rather than FTH1-depleted 4T1/E0771-LM3 cells (Figure 8I). Moreover, after adding *Tdo2*^{high} MF-CM, erastin-induced ROS accumulation was accordingly reduced in parental 4T1/E0771-LM3 cells rather than FTH1-depleted 4T1/E0771-LM3 cells. However, treatment of FTH1-depleted 4T1/E0771-LM3 cells with DFOM (the iron chelator) restricted ROS level in the presence of erastin (Figure 8J), suggesting that KYN could reduce ROS level in DTCs by upregulating FTH1 level. Collectively, these results demonstrated that *Tdo2*^{high} MF-derived KYN upregulated FTH1 level in DTCs, enabling DTCs to resist ferroptosis.

3.8 | *Tdo2*^{high} MFs mediated immune suppression in lung metastasis microenvironment

The aforementioned data demonstrated that the TDO2-KYN axis could directly impact metastasis formation of DTCs. Re-analyzing the scRNA-seq and bulk-seq data of

indicating intracellular Fe^{2+} concentration in the indicated groups (1 μmol/L erastin). (J) ROS levels of tumor cells cultured with indicated CM for 2 days in the presence or absence of 100 μmol/L DFOM and treated with 1 μmol/L erastin, respectively. Results represent mean ± SD. Student's t-test in B and E, one-way ANOVA test in G, two-way ANOVA test in H. $^{**}P < 0.01$; $^{***}P < 0.001$. Abbreviations: DTCs, disseminated tumor cells; *Fth1*/FTH1, ferritin heavy chain 1; qRT-PCR, quantitative real-time polymerase chain reaction; 4T1-LM3, 4T1-lung metastasis 3; E0771-LM3, E0771-lung metastasis 3; CM, conditioned medium; KYN, kynurenine; IHC, immunohistochemistry; liprox, liproxstatin-1; *Tdo2*$^{fl/fl}$, *Tdo2* $^{flox/flox}$; *Tdo2*^{cKO}, *Tdo2* conditioned knockout; shNC, negative control short hairpin RNA; shFTH1, short hairpin RNA of FTH1; ROS, reactive oxygen species; DFOM, deferoxamine mesylate.

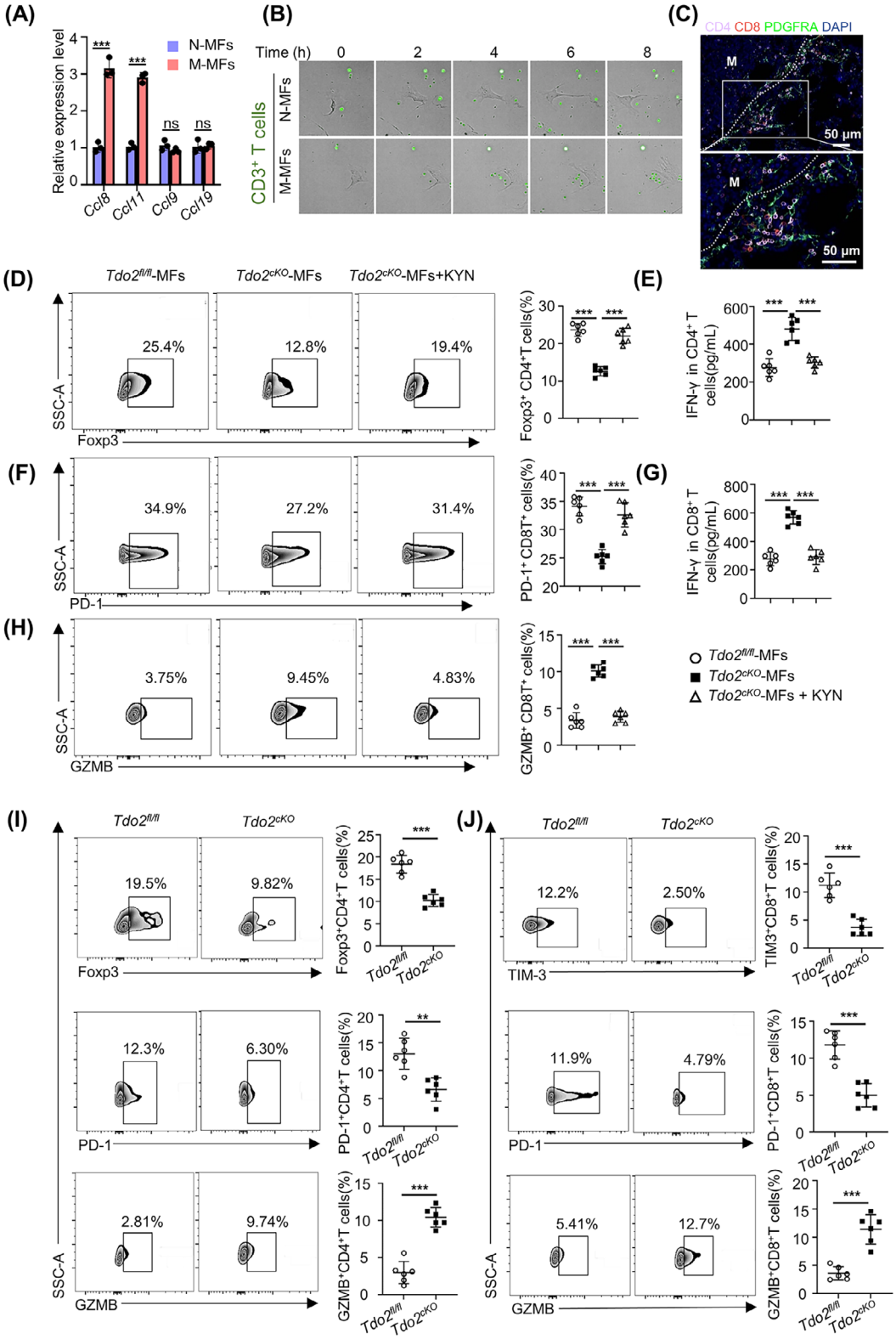

FIGURE 9 *Tdo2*^{high} MFs mediated immune suppression in the lung metastasis microenvironment. (A) qRT-PCR analysis showing expression of *Ccl8*, *Ccl9*, *Ccl11*, and *Ccl19* in M-MFs and N-MFs ($n = 3$). (B) High-content cell imaging showing CD3$^+$ T cell (green) chemoattractant abilities of MFs from normal and metastatic lungs in vitro. (C) MxIF staining for PDGFRA, CD4, CD8 and DAPI in metastatic lung tissue of BALB/c mice. Dashed lines indicate margins of metastatic foci. (D, F and H) Co-culture of MFs from *Tdo2*$^{fl/fl}$ or *Tdo2*^{cKO} mice with T cells (with/without KYN treatment in vitro). Images and quantification of flow cytometry presenting the proportions of Foxp3$^+$CD4$^+$ T cells (D), PD-1$^+$CD8$^+$ T cells (F) and GZMB$^+$CD8$^+$ T cells (H) in the indicated groups ($n = 6$). (E and G) IFN-γ protein levels of CD4$^+$ T cells (E), CD8$^+$ T cells (G) in indicated groups ($n = 6$, measured by ELISA). (I) Images and quantification of flow cytometry

MFs, we noted a significant inflammatory response signaling in MFs (Figure 2I and Figure 3B, Supplementary Figure S5B-C). Moreover, *TDO2* and immunity suppressors (*PD-1*, programmed cell death-ligand 1 [*PD-L1*], cytotoxic T-lymphocyte associated protein 4 [*CTLA4*], *IL-10*) showed positive correlations in lung metastases of breast cancer patients, which was also replicated in lung metastases of colorectal cancer patients (Supplementary Figure S11). There was enhanced expression of T cell chemokine genes (*Ccl8, Ccl11*) in *Tdo2*^{high} MFs (Figure 9A), indicating potential T cell recruitment capacity of *Tdo2*^{high} MFs. Indeed, co-culturing T cells with N-MFs and M-MFs, M-MFs had stronger chemoattractant ability to T cells (green) than N-MFs (Figure 9B; Supplementary videos). Both CD4$^+$ and CD8$^+$ T cells were significantly enriched around MFs, locating on the periphery of metastatic foci (Figure 9C).

Triple-negative breast cancer is known as a "cold" tumor, characterized by the absence or exclusion of T cells in the tumor parenchyma ("immune-desert"/"immune-excluded") [36]; and Trp catabolism has been discovered to affect functions of tumor-infiltrating T cells [37]. These clues raised another exciting scientific hypothesis that *Tdo2*^{high} MFs may participate in the formation of "cold tumor" by preventing T cells from accessing metastatic foci and mediating T-cell suppression in the metastatic niche. To address this intriguing issue, we tried to ascertain whether *Tdo2*^{high} MFs play immunomodulatory roles in infiltrating T cells. Co-culture of MFs from *Tdo2*^{cKO} mice with T cells resulted in Foxp3 downregulation and IFN-γ increase in CD4$^+$ T cells (Figure 9D-E); consistently, PD-1 of CD8$^+$ T cells was decreased (Figure 9F), while the secretion of IFN-γ and GZMB was increased in CD8$^+$ T cells (Figure 9G-H). However, KYN treatment reversed these phenotypes of infiltrating T cells (Figure 9D-H), suggesting that *Tdo2*^{high} MFs potentially suppressed T cell function via KYN. Furthermore, checking the immune-regulatory effects of *Tdo2*^{high} MFs in vivo using lung metastasis mouse models, we found more abundant regulatory T cells (Foxp3$^+$CD4$^+$) in *Tdo2*$^{fl/fl}$ mice than in *Tdo2*^{cKO} mice (Figure 9I). Notable downregulation of PD-1 and increased GZMB were observed in CD4$^+$ T cells from *Tdo2*^{cKO} mice (Figure 9I). Consistently, CD8$^+$ T cells isolated from *Tdo2*^{cKO} mice displayed a dramatic downregulation of TIM-3 and PD-1, and enhanced GZMB (Figure 9J), indicating that depleting *Tdo2* in MFs can partially reverse the exhausted state of intralesional CD8$^+$ T cells and restore their cytotoxic functions. Taken together, these data revealed that TDO2-mediated Trp catabolism in MFs suppressed T cell functions and established a "barrier" to shield tumor cells from T cell attacks, supporting DTCs' immune escape. The schematic diagram of TDO2$^+$ MF-mediated DTCs' ferroptosis resistance and T cell dysfunction is displayed in Figure 10.

4 | DISCUSSION

Organotropic metastasis threatens the lives of breast cancer patients, but the underlying mechanisms remain elusive [38]. Indeed, DTCs and its niche may show interdependent evolutionary paths with more certainty than primary tumors [39, 40], highlighting the important role of metastatic niche in metastasis growth. Here, we used scRNA-seq to illuminate the dynamic characteristic changes of MAF subtypes. Combining various mouse models with survival analysis in patient cohorts, we demonstrated crucial roles of specific crosstalk at metastatic niches among DTCs, T cells, and TDO2$^+$ MFs at single-cell resolutions. The up-regulated expression of *Tdo2* in activated MFs led to abundant secreted KYN production which promoted metastasis growth by significantly improving ferroptosis resistance of DTCs and impairing T cell function.

Stromal heterogeneity possesses the characteristics of time dependence. Our data uncover the temporal molecular features of 3 distinct local lung fibroblast subtypes. Furthermore, signaling pathways associated with fibroblast activation were instigated in a stage-specific manner. Previous studies raised the concept of dynamic tumor microenvironment: genomically stable cells changed their transcriptional program to track the evolving tumor niche. For example, at breast cancer primary sites, CAF subtypes appear to transition from an early immunoregulatory transcriptional program to a late antigen-presentation program [18]. Current understanding of fibroblast activation is mainly limited to primary tumors, and the focus on MAFs is relatively small [41]. Our findings expand this concept to the lung niche. Interestingly, we observed that the endocy-

presenting the proportions of Foxp3$^+$, GZMB$^+$ and PD-1$^+$ CD4$^+$ T cells for indicated groups ($n = 6$). (J) Flow cytometry images and quantification presenting the proportions of TIM-3$^+$, GZMB$^+$ and PD-1$^+$ CD8$^+$ T cells for indicated groups ($n = 6$). Results represent mean ± SD. Student's t-test in A, I and J, others one-way ANOVA. $^{**}P < 0.01$; $^{***}P < 0.001$; ns, not significant. Abbreviations: qRT-PCR, quantitative real-time polymerase chain reaction; M-MFs, MFs from metastatic lung; N-MFs, MFs from normal lung; *Ccl8/9/11/19*, C-C motif chemokine ligand *8/9/11/19*. CD3/4/8, cluster of differentiation 3/4/8; PDGFRA, platelet derived growth factor receptor alpha; DAPI, 4',6-diamidino-2-phenylindole; GZMB, granzyme B; Foxp3, forkheadbox protein 3; PD-1, programmed cell death protein-1; IFN-γ, interferon-gamma; TIM-3, T cell immunoglobulin domain and mucin domain-3; *Tdo2*$^{fl/fl}$, *Tdo2*$^{flox/flox}$; *Tdo2*^{cKO}, *Tdo2* conditioned knockout; KYN, kynurenine; ELISA, enzyme-linked immunosorbent assay.

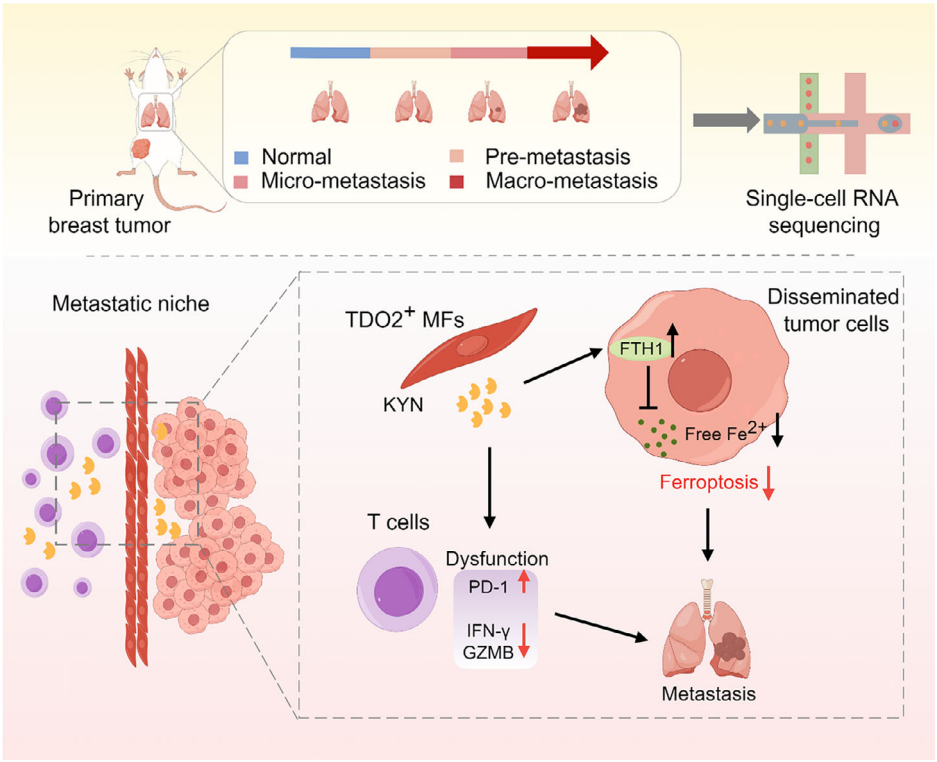

FIGURE 10 The mechanism scheme of TDO2$^+$ MFs in promoting organotropism metastasis of breast cancer. KYN produced by TDO2$^+$ MFs, raised the expression of FTH1 in DTCs, which decreased intracellular accumulation of Fe^{2+} in DTCs to resist ferroptosis. Meanwhile, KYN further promoted T cell dysfunction and mediated DTCs' immune evasion. All the flowcharts were drawn in FigDraw (https://www.figdraw.com/). Abbreviations: TDO2$^+$ MFs, tryptophan 2,3-dioxygenase positive matrix fibroblasts; KYN, kynurenine; FTH1, ferritin heavy chain 1; DTCs, disseminated tumor cells; PD-1, programmed cell death protein-1; IFN-γ, interferon-gamma; GZMB, granzyme B.

tosis programs of LF subtypes (MyoF1 and MyoF2) were instigated early in metastatic stages and persisted functionally, especially in MyoF2. This may explain how breast cancer cells (at the primary site) educated distant resident cells and created a metastases-permissive microenvironment (pre-metastatic niche). For example, in colorectal cancer, primary tumors released extracellular vesicles into the circulation to activate lung fibroblasts [42]; furthermore, exosomes derived from Lewis lung carcinoma (LLC) cells were mainly engulfed by LFs and led to NF-κB activation of fibroblasts [43]. These studies supported our hypothesis about how distant stromal cell subtypes were activated before tumor cells' arrival. Once DTCs arrive at second sites, fibroblasts and immune cells will be further educated and help DTCs settle in the new environment [44, 45], which promotes the generation of heterogeneity and dynamic change of metastatic microenvironment.

Heterogeneous LFs are hijacked by DTCs to facilitate metastasis. ECM remodeling in the metastatic niche was one of the earliest events in metastasis formation and was correlated with immune cell motility in melanoma [46, 47]. Factors secreted by MAFs (e.g., hyaluronic acid) can promote DTCs proliferation [48, 49]. Additionally, MAFs maintain DTCs "stemness" potential by augmenting WNT signaling in metastatic niche [10]. However, these studies have not considered the heterogeneity of fibroblasts. This may explain why CAFs/MAFs targeting has presented positive results in pre-clinical researches while subsequent clinical studies have yielded conflicting results. Therefore, more efforts are needed to describe aspects of their biology to inform treatment decisions [41]. Our results suggested that lung MAFs included three subtypes and that the tumor promoting effects of MFs were multifaceted. Our study provided insights into the versatility of a single subtype, revealing a possible mechanism of "cold tumor" formation in breast cancer.

Growing evidence indicates that metabolic reprogramming of tumors occurs not only within tumor cells, but also in the stromal cells [50, 51]. Because tumor cells are often in a hypoxic and nutrient-deficient environment, tumor cells are mainly anabolic, while CAFs are mainly catabolic [52]. The current study demonstrated that TDO2-mediated Trp catabolism in MFs regulated DTCs to adapt to microenvironment with higher ferroptotic stress and support the formation of immunosuppression. The conclusion is supported by previous work, suggesting that the catabolism of CAFs and the tumor cell metabolism are coupled and that catabolism of CAFs can provide important metabolic sub-

stance for tumor cell growth [53, 54]. Tumor cells and CAFs mutually promote metabolic reprogramming, establishing a symbiotic relationship. Thus, targeting metabolic regulation of MAF subtypes may serve as a promising approach to suppress metastasis formation.

This study also had certain limitations. For instance, we did not explore the mechanisms underlying the upregulation of Tdo2 in MFs. Moreover, how KYN mediates T cell dysfunction needs further investigation. Besides, more studies are needed to determine MyoFs' functions in metastatic progression.

5 | CONCLUSIONS

In conclusion, our findings delineate a multifaceted cellular crosstalk within growing lung metastases of breast cancer. The results show a crucial role for *Tdo2*^{high} MFs during metastatic progression and emphasize the role of Trp catabolism in DTC survival and immunosuppression formation. These interactions in metastatic nodules may serve as useful targets when developing future therapies against metastatic disease.

AUTHOR CONTRIBUTIONS

Yongcan Liu, Shanchun Chen, Yong Teng, Xueying Wan and Manran Liu designed this study; Yongcan Liu, Rui-Wang, Haojun Luo, Chao Chang, Peijin Dai, Yubi Gan, and Yuetong Guo conducted the experiments; Yongcan Liu, Yixuan Hou and Yan Sun analyzed the data; Shanchun Chen drafted the initial manuscript; Yubi Gan, Xiaojiang Cui and Manran Liu revised this manuscript; all authors read and approved the final manuscript.

ACKNOWLEDGEMENTS

Special thanks to Prof. Suling Liu from Fudan University for help with animal experiments. This work was supported by National Key Projects of Ministry of Science and Technology of China (MOST 2018YFE0113700), National Natural Science Foundation of China (NSFC82173155, NSFC81874199), and the Outstanding Professorship Program of Chongqing Medical University (2019-R10005) to Manran Liu. This work was also supported by the Outstanding Postgraduate Fund of Chongqing Medical University (BJRC202021, BJRC202025) and the Chongqing Graduate Research and Innovation Project of the Chongqing Education Committee (CYB22218) for Shanchun Chen.

CONFLICT OF INTEREST STATEMENT

The authors declare that they have no competing interests.

DATA AVAILABILITY STATEMENT

The data and materials could be available from the corresponding author upon reasonable request. Bulk RNA-seq data in the study was deposited into GEO with accession number of GSE269817 and GSE270152 (https://www.ncbi.nlm.nih.gov/geo/). scRNA-seq data have been deposited in the Genome Sequence Archive (Genomics, Proteomics & Bioinformatics 2021) in National Genomics Data Center (Nucleic Acids Res 2022), China National Center for Bioinformation/Beijing Institute of Genomics, Chinese Academy of Sciences (GSA: CRA014233) that are publicly accessible at https://ngdc.cncb.ac.cn/gsa.

ETHICS APPROVAL AND CONSENT TO PARTICIPATE

Sample collection and animal experiments were approved by the Ethics Committee of Chongqing Medical University and conducted according to the guidelines for the Care and Use of Laboratory Animals of Chongqing Medical University (2021084).

ORCID

Yongcan Liu https://orcid.org/0009-0001-6698-5282
Haojun Luo https://orcid.org/0000-0002-6860-0251
Xiaojiang Cui https://orcid.org/0000-0002-6843-736X
Manran Liu https://orcid.org/0000-0002-3898-6878

REFERENCES

1. Gerstberger S, Jiang Q, Ganesh K. Metastasis. Cell. 2023;186(8):1564-79.
2. Gao Y, Bado I, Wang H, Zhang W, Rosen J, Zhang X. Metastasis Organotropism: Redefining the Congenial Soil. Dev Cell. 2019;49(3):375-91.
3. Ma T, Tang Y, Wang T, Yang Y, Zhang Y, Wang R, et al. Chronic pulmonary bacterial infection facilitates breast cancer lung metastasis by recruiting tumor-promoting MHCII(hi) neutrophils. Signal Transduct Target Ther. 2023;8(1):296.
4. Gao Y, Wang Y, He B, Pan Y, Zhou D, Xiong M, et al. An Enzyme-Loaded Metal-Organic Framework-Assisted Microfluidic Platform Enables Single-Cell Metabolite Analysis. Angew Chem Int Ed Engl. 2023;62(31):e202302000.
5. Alvarez S, Sviderskiy V, Terzi E, Papagiannakopoulos T, Moreira A, Adams S, et al. NFS1 undergoes positive selection in lung tumours and protects cells from ferroptosis. Nature. 2017;551(7682):639-43.
6. Ubellacker J, Tasdogan A, Ramesh V, Shen B, Mitchell E, Martin-Sandoval M, et al. Lymph protects metastasizing melanoma cells from ferroptosis. Nature. 2020;585(7823):113-8.
7. Joyce JA, Pollard JW. Microenvironmental regulation of metastasis. Nat Rev Cancer. 2009;9(4):239-52.
8. Shen Y, Wang X, Lu J, Salfenmoser M, Wirsik N, Schleussner N, et al. Reduction of Liver Metastasis Stiffness Improves Response to Bevacizumab in Metastatic Colorectal Cancer. Cancer Cell. 2020;37(6):800-17.e7.
9. Pein M, Insua-Rodríguez J, Hongu T, Riedel A, Meier J, Wiedmann L, et al. Metastasis-initiating cells induce and exploit a fibroblast niche to fuel malignant colonization of the lungs. Nat Commun. 2020;11(1):1494.
10. Malanchi I, Santamaria-Martínez A, Susanto E, Peng H, Lehr H, Delaloye J, et al. Interactions between cancer stem cells and their

niche govern metastatic colonization. Nature. 2011;481(7379):85-9.
11. Shani O, Vorobyov T, Monteran L, Lavie D, Cohen N, Raz Y, et al. Fibroblast-Derived IL33 Facilitates Breast Cancer Metastasis by Modifying the Immune Microenvironment and Driving Type 2 Immunity. Cancer Res. 2020;80(23):5317-29.
12. Gong Z, Li Q, Shi J, Wei J, Li P, Chang C, et al. Lung fibroblasts facilitate pre-metastatic niche formation by remodeling the local immune microenvironment. Immunity. 2022;55(8):1483-500.e9.
13. Wang Q, Ding Y, Song P, Zhu H, Okon I, Ding YN, et al. Tryptophan-Derived 3-Hydroxyanthranilic Acid Contributes to Angiotensin II-Induced Abdominal Aortic Aneurysm Formation in Mice In Vivo. Circulation. 2017;136(23):2271-83.
14. Liu X, Geng Y, Liang J, Coelho A, Yao C, Deng N, et al. HER2 drives lung fibrosis by activating a metastatic cancer signature in invasive lung fibroblasts. J Exp Med. 2022;219(10):e20220126.
15. Zheng Z, Li Y, Jia S, Zhu M, Cao L, Tao M, et al. Lung mesenchymal stromal cells influenced by Th2 cytokines mobilize neutrophils and facilitate metastasis by producing complement C3. Nat Commun. 2021;12(1):6202.
16. Haj-Shomaly J, Vorontsova A, Barenholz-Cohen T, Levi-Galibov O, Devarasetty M, Timaner M, et al. T Cells Promote Metastasis by Regulating Extracellular Matrix Remodeling following Chemotherapy. Cancer Res. 2022;82(2):278-91.
17. Lendahl U, Muhl L, Betsholtz C. Identification, discrimination and heterogeneity of fibroblasts. Nat Commun. 2022;13(1):3409.
18. Friedman G, Levi-Galibov O, David E, Bornstein C, Giladi A, Dadiani M, et al. Cancer-associated fibroblast compositions change with breast cancer progression linking the ratio of S100A4(+) and PDPN(+) CAFs to clinical outcome. Nat Cancer. 2020;1(7):692-708.
19. Affo S, Nair A, Brundu F, Ravichandra A, Bhattacharjee S, Matsuda M, et al. Promotion of cholangiocarcinoma growth by diverse cancer-associated fibroblast subpopulations. Cancer Cell. 2021;39(6):866-82.e11.
20. Zhang M, Yang H, Wan L, Wang Z, Wang H, Ge C, et al. Single-cell transcriptomic architecture and intercellular crosstalk of human intrahepatic cholangiocarcinoma. J Hepatol. 2020;73(5):1118-30.
21. Xie T, Wang Y, Deng N, Huang G, Taghavifar F, Geng Y, et al. Single-Cell Deconvolution of Fibroblast Heterogeneity in Mouse Pulmonary Fibrosis. Cell Rep. 2018;22(13):3625-40.
22. Tahara RK, Brewer TM, Theriault RL, Ueno NT. Bone Metastasis of Breast Cancer. Adv Exp Med Biol. 2019;1152:105-29.
23. Chen K, Wang Q, Li M, Guo H, Liu W, Wang F, et al. Single-cell RNA-seq reveals dynamic change in tumor microenvironment during pancreatic ductal adenocarcinoma malignant progression. EBioMedicine. 2021;66:103315.
24. Li P, Lu M, Shi J, Gong Z, Hua L, Li Q, et al. Lung mesenchymal cells elicit lipid storage in neutrophils that fuel breast cancer lung metastasis. Nat Immunol. 2020;21(11):1444-55.
25. Hu S, Lu H, Xie W, Wang D, Shan Z, Xing X, et al. TDO2+ myofibroblasts mediate immune suppression in malignant transformation of squamous cell carcinoma. J Clin Invest. 2022;132(19):e157649.
26. Lee R, Li J, Li J, Wu C, Jiang S, Hsu W, et al. Synthetic Essentiality of Tryptophan 2,3-Dioxygenase 2 in APC-Mutated Colorectal Cancer. Cancer Discov. 2022;12(7):1702-17.
27. Galán-Díez M, Borot F, Ali AM, Zhao J, Gil-Iturbe E, Shan X, et al. Subversion of Serotonin Receptor Signaling in Osteoblasts by Kynurenine Drives Acute Myeloid Leukemia. Cancer Discov. 2022;12(4):1106-27.
28. Xue C, Li G, Zheng Q, Gu X, Shi Q, Su Y, et al. Tryptophan metabolism in health and disease. Cell Metab. 2023;35(8):1304-26.
29. Platten M, Nollen EAA, Röhrig UF, Fallarino F, Opitz CA. Tryptophan metabolism as a common therapeutic target in cancer, neurodegeneration and beyond. Nat Rev Drug Discov. 2019;18(5):379-401.
30. Wu M, Zhang X, Zhang W, Chiou Y, Qian W, Liu X, et al. Cancer stem cell regulated phenotypic plasticity protects metastasized cancer cells from ferroptosis. Nat Commun. 2022;13(1):1371.
31. Fiore A, Zeitler L, Russier M, Groß A, Hiller M, Parker J, et al. Kynurenine importation by SLC7A11 propagates anti-ferroptotic signaling. Mol Cell. 2022;82(5):920-32.e7.
32. Stockwell B, Friedmann Angeli J, Bayir H, Bush A, Conrad M, Dixon S, et al. Ferroptosis: A Regulated Cell Death Nexus Linking Metabolism, Redox Biology, and Disease. Cell. 2017;171(2):273-85.
33. Liu L, Zheng B, Luo M, Du J, Yang F, Huang C, et al. Suppression of USP8 sensitizes cells to ferroptosis via SQSTM1/p62-mediated ferritinophagy. Protein Cell. 2023;14(3):230-4.
34. Deng GH, Wu CF, Li YJ, Shi H, Zhong WC, Hong MK, et al. Caveolin-1 is critical for hepatic iron storage capacity in the development of nonalcoholic fatty liver disease. Mil Med Res. 2023;10(1):53.
35. Guo QL, Dai XL, Yin MY, Cheng HW, Qian HS, Wang H, et al. Nanosensitizers for sonodynamic therapy for glioblastoma multiforme: current progress and future perspectives. Mil Med Res. 2022;9(1):26.
36. Zhang J, Huang D, Saw P, Song E. Turning cold tumors hot: from molecular mechanisms to clinical applications. Trends Immunol. 2022;43(7):523-45.
37. Shi D, Wu X, Jian Y, Wang J, Huang C, Mo S, et al. USP14 promotes tryptophan metabolism and immune suppression by stabilizing IDO1 in colorectal cancer. Nat Commun. 2022;13(1):5644.
38. Jiang B, Zhao X, Chen W, Diao W, Ding M, Qin H, et al. Lysosomal protein transmembrane 5 promotes lung-specific metastasis by regulating BMPR1A lysosomal degradation. Nat Commun. 2022;13(1):4141.
39. Dang H, Krasnick B, White B, Grossman J, Strand M, Zhang J, et al. The clonal evolution of metastatic colorectal cancer. Sci Adv. 2020;6(24):eaay9691.
40. Birkbak N, McGranahan N. Cancer Genome Evolutionary Trajectories in Metastasis. Cancer Cell. 2020;37(1):8-19.
41. Caligiuri G, Tuveson D. Activated fibroblasts in cancer: Perspectives and challenges. Cancer Cell. 2023;41(3):434-49.
42. Ji Q, Zhou L, Sui H, Yang L, Wu X, Song Q, et al. Primary tumors release ITGBL1-rich extracellular vesicles to promote distal metastatic tumor growth through fibroblast-niche formation. Nat Commun. 2020;11(1):1211.
43. Du C, Duan X, Yao X, Wan J, Cheng Y, Wang Y, et al. Tumour-derived exosomal miR-3473b promotes lung tumour cell intrapulmonary colonization by activating the nuclear factor-κB of local fibroblasts. J Cell Mol Med. 2020;24(14):7802-13.

44. Zarrer J, Haider MT, Smit DJ, Taipaleenmäki H. Pathological Crosstalk between Metastatic Breast Cancer Cells and the Bone Microenvironment. Biomolecules. 2020;10(2): 337.
45. Li P, Lu M, Shi J, Gong Z, Hua L, Li Q, et al. Lung mesenchymal cells elicit lipid storage in neutrophils that fuel breast cancer lung metastasis. Nat Immunol. 2020;21(11):1444-55.
46. Shani O, Raz Y, Monteran L, Scharff Y, Levi-Galibov O, Megides O, et al. Evolution of fibroblasts in the lung metastatic microenvironment is driven by stage-specific transcriptional plasticity. Elife. 2021;10:e60745.
47. Kaur A, Ecker B, Douglass S, Kugel C, Webster M, Almeida F, et al. Remodeling of the Collagen Matrix in Aging Skin Promotes Melanoma Metastasis and Affects Immune Cell Motility. Cancer Discov. 2019;9(1):64-81.
48. Bhattacharjee S, Hamberger F, Ravichandra A, Miller M, Nair A, Affo S, et al. Tumor restriction by type I collagen opposes tumor-promoting effects of cancer-associated fibroblasts. J Clin Invest. 2021;131(11):e146987.
49. Shimizu S, Yamada N, Sawada T, Ikeda K, Kawada N, Seki S, et al. In vivo and in vitro interactions between human colon carcinoma cells and hepatic stellate cells. Jpn J Cancer Res: Gann. 2000;91(12):1285-95.
50. Faubert B, Solmonson A, DeBerardinis RJ. Metabolic reprogramming and cancer progression. Science. 2020;368(6487) :eaaw5473.
51. Zhang W, Bouchard G, Yu A, Shafiq M, Jamali M, Shrager JB, et al. GFPT2-Expressing Cancer-Associated Fibroblasts Mediate Metabolic Reprogramming in Human Lung Adenocarcinoma. Cancer Res. 2018;78(13):3445-57.
52. Mishra R, Haldar S, Placencio V, Madhav A, Rohena-Rivera K, Agarwal P, et al. Stromal epigenetic alterations drive metabolic and neuroendocrine prostate cancer reprogramming. J Clin Invest. 2018;128(10):4472-84.
53. Avagliano A, Granato G, Ruocco MR, Romano V, Belviso I, Carfora A, et al. Metabolic Reprogramming of Cancer Associated Fibroblasts: The Slavery of Stromal Fibroblasts. Biomed Res Int. 2018;2018:6075403.
54. Wu D, Zhuo L, Wang X. Metabolic reprogramming of carcinoma-associated fibroblasts and its impact on metabolic heterogeneity of tumors. Semin Cell Dev Biol. 2017;64:125-31.

SUPPORTING INFORMATION

Additional supporting information can be found online in the Supporting Information section at the end of this article.

How to cite this article: Liu Y, Chen S, Wan X, Wang R, Luo H, Chang C, et al. Tryptophan 2,3-dioxygenase-positive matrix fibroblasts fuel breast cancer lung metastasis via kynurenine-mediated ferroptosis resistance of metastatic cells and T cell dysfunction. Cancer Commun.. 2024;1–26.
https://doi.org/10.1002/cac2.12608